

# STELLAR KINEMATICS IN THE COMPLICATED INNER SPHEROID OF M31: DISCOVERY OF SUBSTRUCTURE ALONG THE SOUTHEASTERN MINOR AXIS AND ITS RELATIONSHIP TO THE GIANT SOUTHERN STREAM

KAROLINE M. GILBERT<sup>1</sup>, MARK FARDAL<sup>2</sup>, JASONJOT S. KALIRAI<sup>1,3</sup>, PURAGRA GUHATHAKURTA<sup>1</sup>, MARLA C. GEHA<sup>4,5</sup>, JEDIDAH ISLER<sup>6,7</sup>, STEVEN R. MAJEWSKI<sup>8</sup>, JAMES C. OSTHEIMER<sup>8</sup>, RICHARD J. PATTERSON<sup>8</sup>, DAVID B. REITZEL<sup>9</sup>, EVAN KIRBY<sup>1</sup>, AND MICHAEL C. COOPER<sup>10</sup>

*Accepted for publication in ApJ, June 23 2007*

## ABSTRACT

We present the discovery of a kinematically-cold stellar population along the southeastern minor axis of the Andromeda galaxy (M31) that is likely the forward continuation of M31's giant southern stream. This discovery was made in the course of an on-going spectroscopic survey of red giant branch (RGB) stars in M31 using the DEIMOS instrument on the Keck II 10-m telescope<sup>11</sup>. Stellar kinematics are investigated in eight fields located 9–30 kpc from M31's center (in projection). A likelihood method based on photometric and spectroscopic diagnostics is used to isolate confirmed M31 RGB stars from foreground Milky Way dwarf stars: for the first time, this is done *without* using radial velocity as a selection criterion, allowing an unbiased study of M31's stellar kinematics. The radial velocity distribution of the 1013 M31 RGB stars shows evidence for the presence of two components. The broad (hot) component has a velocity dispersion of  $\sigma_v^{\text{sph}} = 129 \text{ km s}^{-1}$  and presumably represents M31's virialized spheroid. A significant fraction (19%) of the population is in a narrow (cold) component centered near M31's systemic velocity with a velocity dispersion that decreases with increasing radial distance, from  $\sigma_v^{\text{sub}} = 55.5 \text{ km s}^{-1}$  at  $R_{\text{proj}} = 12 \text{ kpc}$  to  $\sigma_v^{\text{sub}} = 10.6 \text{ km s}^{-1}$  (an *intrinsic* velocity dispersion of  $9.5 \text{ km s}^{-1}$  after accounting for velocity measurement error) at  $R_{\text{proj}} = 18 \text{ kpc}$ . The spatial and velocity distribution of the cold component matches that of the "Southeast shelf" predicted by the Fardal et al. (2007) orbital model of the progenitor of the giant southern stream. The metallicity distribution of the cold component matches that of the giant southern stream, but is about 0.2 dex more metal rich on average than that of the hot spheroidal component. We discuss the implications of our discovery on the interpretation of the intermediate-age spheroid population found in this region in recent ultra-deep *HST* imaging studies.

*Subject headings:* galaxies: substructure — galaxies: halo — galaxies: individual (M31) — stars: kinematics — techniques: spectroscopic

## 1. INTRODUCTION

Electronic address: kgilbert@ucolick.org,  
fardal@fcrao1.astro.umass.edu, jkalirai@ucolick.org,  
raja@ucolick.org, marla.geha@nrc-cnrc.gc.ca, jcisler@ucolick.org,  
srm4n@virginia.edu, jostheim@alumni.virginia.edu,  
rjp0i@virginia.edu, reitzel@astro.ucla.edu, ekirby@ucolick.org,  
cooper@astron.berkeley.edu

<sup>1</sup>UCO/Lick Observatory, Department of Astronomy & Astrophysics, University of California Santa Cruz, 1156 High Street, Santa Cruz, California 95064.

<sup>2</sup>Department of Astronomy, University of Massachusetts, Amherst, Massachusetts 01003.

<sup>3</sup>Hubble Fellow.

<sup>4</sup>NRC Herzberg Institute of Astrophysics, 5701 West Saanich Road, Victoria, British Columbia, Canada V9E 2E7.

<sup>5</sup>Plaskett Fellow.

<sup>6</sup>Fisk University/Vanderbilt University, Nashville, Tennessee 37325.

<sup>7</sup>Visiting Student, University of California Santa Cruz.

<sup>8</sup>Department of Astronomy, University of Virginia, PO Box 400325, Charlottesville, VA 22904-4325.

<sup>9</sup>Department of Physics & Astronomy, Knudsen Hall, University of California, Los Angeles, California 90095.

<sup>10</sup>Department of Astronomy, Campbell Hall, University of California, Berkeley, California 94720.

<sup>11</sup>Data presented herein were obtained at the W. M. Keck Observatory, which is operated as a scientific partnership among the California Institute of Technology, the University of California and the National Aeronautics and Space Administration. The Observatory was made possible by the generous financial support of the W. M. Keck Foundation.

In the current paradigm of hierarchical galaxy formation, massive galaxies are built up through a series of major and minor merger events (Searle & Zinn 1978; White & Rees 1978). Observations of galaxies at high redshift show that merging systems are common (e.g., Abraham et al. 1996; LeFevre et al. 2000; Conselice et al. 2003; Lotz et al. 2007), and large-scale simulations of galaxy formation in a cosmological context have successfully reproduced many of the observed properties of galaxies and galaxy clusters (e.g., Springel et al. 2005; Croton et al. 2006).

A consequence of hierarchical galaxy formation is that galactic stellar halos should be at least partially composed of the tidal debris from past accretion events. Numerical simulations and semi-analytic models of stellar halo formation have made great strides toward understanding the properties of halos that are built up through tidal stripping of merging systems (e.g., Johnston et al. 1996; Johnston 1998; Helmi & White 1999; Helmi & de Zeeuw 2000; Bullock et al. 2001; Bullock & Johnston 2005). Detailed comparisons between observations and simulations are needed to determine the fraction of stellar halos that are made up of tidal debris and to better understand the formation of galaxies in general.

Recent discoveries of tidal streams in the stellar halos of the Milky Way (MW) and Andromeda (M31) galaxies

are providing the most direct and detailed observational constraints on theories of stellar halo formation. Among the most prominent of these substructures are the Sagittarius stream (Ibata et al. 1994; Majewski et al. 2003; Newberg et al. 2003), the Monoceros stream (Yanny et al. 2003; Rocha-Pinto et al. 2003), and the Magellanic stream (Mathewson et al. 1974) in the MW, and the giant southern stream (GSS; Ibata et al. 2001b) in M31. Additional substructures have been identified in M31 that are also likely remnants of past mergers, such as the Northeast shelf (Ferguson et al. 2002; Ibata et al. 2004; Fardal et al. 2006), a secondary cold component in the same physical location as the giant southern stream (Kalirai et al. 2006a), and the various substructures identified with the disk of M31 (Ibata et al. 2005). Tidal disruption has also been observed in M31’s satellite galaxies M32 and NGC 205 (Choi et al. 2002).

In addition to providing insight into theoretical models of stellar halo formation, the observed properties of tidal streams can be used to constrain the galactic potential in which they are found if sufficient phase-space information is available (e.g., Johnston et al. 1999, 2002; Peñarrubia et al. 2006). Several attempts have been made to model the mass distribution of the MW using observed substructure, most of which have focused on the orbital properties of the Sagittarius stream (e.g., Ibata et al. 2001a; Helmi 2004; Martínez-Delgado et al. 2004; Johnston et al. 2005; Law et al. 2005; Fellhauer et al. 2006).

The GSS has been the focus of detailed modeling in M31, spurred on by recent observations. Imaging and photometry have revealed the physical extent of the GSS (Ferguson et al. 2002; McConnachie et al. 2003; Ferguson et al. 2006) and provided line-of-sight distances at various points along it (McConnachie et al. 2003), while spectroscopy has yielded the mean line-of-sight velocity and velocity dispersion of stream stars as a function of position (Ibata et al. 2004; Guhathakurta et al. 2006; Kalirai et al. 2006a). The availability of this phase-space information has motivated several groups to model the orbit of the progenitor of the GSS (Ibata et al. 2004; Font et al. 2006; Fardal et al. 2006, 2007). However, Fardal et al. (2006) concluded that the degree to which the GSS can be used to constrain M31’s mass distribution is limited by the current measurement uncertainties in the distance to the stream and the lack of a clearly identified compact stellar concentration that might correspond to the dense remnant core of the stream’s progenitor galaxy. Further observational constraints on the orbit of the progenitor of the GSS, such as the identification of tidal debris from other pericentric passages, are needed to make progress.

Towards this end, Fardal et al. (2007, hereafter F07) show that several of the observed features in M31 can be explained as the forward continuation of the GSS. Their model makes predictions that can be tested by observations, including the stellar velocity distributions in the Northeast and Western shelves and the presence of a weaker shelf on the eastern side of the galaxy. This last shelf is expected to be most easily visible near the southeastern minor axis of M31<sup>12</sup>.

<sup>12</sup> Although this shell feature is expected to span an  $\sim 180^\circ$  range in position angle, covering the eastern half of the galaxy, it is expected to be most easily observable in the southeast due

This paper presents new substructure along M31’s southeastern minor axis at the expected location of the F07 Southeast shelf and displaying the distinct kinematic profile predicted by their orbital model. The substructure was discovered in the course of an on-going Keck/DEIMOS spectroscopic study of the dynamics and metallicity of RGB stars in the inner spheroid and outer halo of M31 (see Gilbert et al. 2006, and references therein). The portion of the inner spheroid studied here appeared to be relatively undisturbed in earlier star count maps (Ferguson et al. 2002) and radial velocity surveys (Reitzel & Guhathakurta 2002; Kalirai et al. 2006a). The photometric and spectroscopic data used in this analysis are described in § 2. The criteria for selection of M31 RGB stars are discussed in § 3. The kinematics of the RGB population (first the combined data set and then the individual fields) are characterized in § 4. The spatial trends and general properties of the dynamically hot spheroid and cold substructure populations are discussed in § 5 and § 6, respectively. The physical origin of the cold substructure is explored in § 7, including its likely relation to M31’s GSS. The relevance of the newly discovered cold substructure to the Brown et al. (2003) discovery of an intermediate-age population in the spheroid of M31 is discussed § 8. The main conclusions of the paper are summarized in § 9.

## 2. DATA

The data set discussed in this paper is drawn from photometry and spectroscopy of several fields on/near the southeastern minor axis of M31. The locations of the fields are shown in Figures 1 and 2. They span a range of projected radial distances from M31’s center of  $R_{\text{proj}} \sim 9$  to 30 kpc (Table 1). A brief explanation of the data sets and reduction is included below. A more detailed discussion of the observational strategy and data reduction methods employed in our M31 survey can be found in Guhathakurta et al. (2006), Kalirai et al. (2006a,b), and Gilbert et al. (2006).

### 2.1. Photometry

Photometry and astrometry for the majority of the fields analysed in this paper were derived from MegaCam images in the  $g'$  and  $i'$  bands obtained with the 3.6-m Canada-France-Hawaii Telescope (CFHT)<sup>13</sup>. The program SExtractor (Bertin & Arnouts 1996) was used for object detection, photometry, and morphological classification (via the `stellarity` parameter). The instrumental  $g'$  and  $i'$  magnitudes were transformed to Johnson-Cousins  $V$  and  $I$  magnitudes based on observations of Landolt photometric standard stars (Kalirai et al. 2006a).

Photometry and astrometry for a0, the outermost field discussed in this paper, were derived by Ostheimer (2002) from images obtained with the Mosaic camera on the Kitt Peak National Observatory (KPNO)<sup>14</sup> 4-m tele-

to overlap with the much denser Northeast shelf and M31’s disk elsewhere (see Fig. 12).

<sup>13</sup> MegaPrime/MegaCam is a joint project of CFHT and CEA/DAPNIA, at the Canada-France-Hawaii Telescope which is operated by the National Research Council of Canada, the Institut National des Science de l’Univers of the Centre National de la Recherche Scientifique of France, and the University of Hawaii.

<sup>14</sup> Kitt Peak National Observatory of the National Optical As-

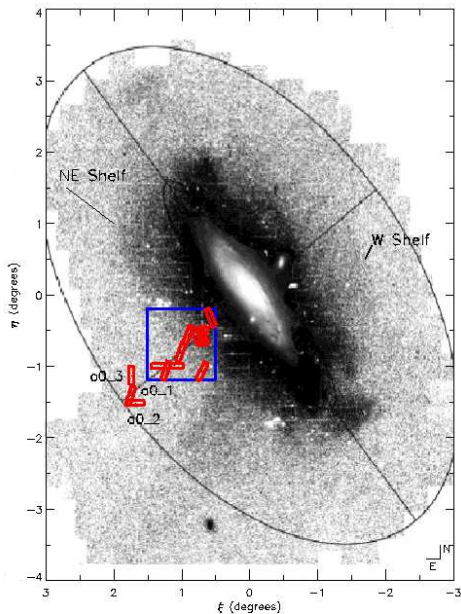


FIG. 1.— Sky positions of the fields discussed in this paper. The blue square represents the position and area of the CFHT/MegaCam image (Fig. 2). The red rectangles approximate the size and position angle of the DEIMOS spectroscopic slitmasks. The three masks nearest the outer ellipse are in field a0. The remaining masks are identified in Figure 2. The star count map comes from Ibata et al. (2005), and is in standard M31-centric coordinates  $(\xi, \eta)$ . The outer ellipse represents a 55 kpc radius along the major axis, with a flattening of 3:5. The major and minor axes of M31 are indicated by straight lines. The giant southern stream is the obvious overdensity of stars south of M31’s center.

scope in the Washington System  $M$  and  $T_2$  bands and the intermediate-width DDO51 band. This combination of filters allows photometric selection of stars that are likely to be M31 red giant branch (RGB) stars rather than MW dwarf stars (e.g., Palma et al. 2003; Majewski et al. 2005). The DDO51 filter is centered at a wavelength of 5150 Å with a width of  $\sim 100$  Å, and includes the surface-gravity sensitive Mg  $b$  and MgH stellar absorption features which are strong in dwarf stars but weak in RGB stars. Based on a star’s position in the  $(M - DDO51)$  versus  $(M - T_2)$  color-color diagram, it is assigned a probability of being an M31 RGB star. Johnson-Cousins  $V$  and  $I$  magnitudes were derived from the  $M$  and  $T_2$  magnitudes using the photometric transformation relations in Majewski et al. (2000). Use of DDO51 photometry to screen for likely M31 RGB stars increases the efficiency of the spectroscopic observations, suppressing the number of selected MW dwarf stars by a factor of  $\approx 3$  in a0 (Guhathakurta et al. 2007, in prep).

## 2.2. Spectroscopy

### 2.2.1. Slitmask Design and Observations

Objects in fields covered by the CFHT/MegaCam images were selected for Keck/DEIMOS spectroscopy based on  $I$  magnitude and the SExtractor morphological criterion `stellarity` (Kalirai et al. 2006a). Objects in field a0 were selected on the basis of  $I$  magnitude and morphological criteria (DAOPHOT parameters `chi` and `sharp`),

tronomy Observatory is operated by the Association of Universities for Research in Astronomy, Inc., under cooperative agreement with the National Science Foundation.

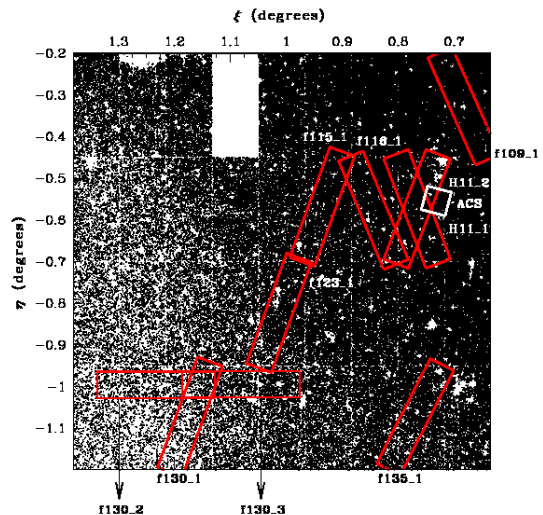


FIG. 2.— Starcount map derived from CFHT/MegaCam photometry in a single pointing with the 36-CCD mosaic (§ 2.1). The orientation of this map is the same as Figure 1. The size and positions of the masks designed from the CFHT/MegaCam photometry are shown as red rectangles. The white square shows the position and approximate orientation of the Brown et al. (2003) deep HST/ACS observations (§ 8). The three a0 masks were based on photometry from the KPNO 4-m telescope and are to the south-east (bottom left), beyond the limit of this image. There is an apparent edge in the density of star counts in the image, running from the upper left to the lower right and passing through field f123; this feature will be discussed in § 7.1.

prioritized according to their probability of being an M31 RGB star (based on  $M$ ,  $T_2$ , and DDO51 photometry as described in § 2.1). Pre-selection of likely M31 RGB stars is vital for efficient study of the sparse outer parts of the M31 halo. The inner fields (such as the fields drawn from the CFHT/MegaCam images) contain a relatively high surface density of M31 RGB stars, so the RGB to MW dwarf star ratio is high even without DDO51-based pre-selection of RGB candidates.

For the purposes of most of the analysis in this paper, data are classified according to fields, rather than spectroscopic masks. In general, a “field” refers to the area covered by a single CFHT/MegaCam CCD ( $\sim 15' \times 6'5$ , Fig. 2); there can be one or more overlapping DEIMOS masks ( $16' \times 4'$ ) in a single field. For example, masks H11.1 and H11.2 are both part of field H11. There are two exceptions to this field/mask scheme: (1) the a0 field refers to a single Mosaic pointing, which covers a  $35' \times 35'$  area, and (2) two of the f130 masks each straddle a couple of adjacent MegaCam CCDs, but since they were chosen to overlap with the f130\_1 mask, they have been labelled f130\_2 and f130\_3.

Fields were observed using the Keck II telescope and the DEIMOS instrument with the 1200 line  $\text{mm}^{-1}$  grating. Most of the fields were observed in Fall 2005 [f109, f115, f116, f123, f130 (1 mask), and f135]. The a0 masks were observed in Fall 2002 and 2004, the H11 masks in 2004, and the last two of the three f130 masks in Fall 2006 (Table 1). The central wavelength for most masks was  $\lambda 7800$  Å, yielding a spectral coverage of approximately  $\lambda \lambda 6450\text{--}9150$  Å. The only exceptions were the a0\_1 and a0\_2 masks observed in 2002, which had a central wavelength of  $\lambda 8550$  Å and a spectral coverage of approx-

imately  $\lambda\lambda 7200\text{--}9900 \text{ \AA}$ . The 1200 line  $\text{mm}^{-1}$  grating has a dispersion of  $0.33 \text{ \AA pix}^{-1}$ ; the scale in the spatial direction is  $0''.12 \text{ pix}^{-1}$ , and the effective scale in the dispersion direction is  $0''.21 \text{ pix}^{-1}$ . Slits had a width of  $1''$ . The spectral resolution for a star observed in typical  $0.8''$  seeing conditions is about  $1.3 \text{ \AA FWHM}$ . Each mask was observed for a total of 1 hour, with the exception of field f109 which was observed for 3 hours.

### 2.2.2. Spectroscopic Data Reduction

The spectra were reduced and analyzed using a modified version of the `spec2d` and `spec1d` software developed by the DEEP2 team at the University of California, Berkeley<sup>15</sup>; these routines perform standard spectral reduction steps, including flat-fielding, night-sky emission line removal, and extraction of the two-dimensional spectra. Reduced one-dimensional spectra are cross-correlated with a library of template stellar spectra to determine the redshift of the object. Each spectrum was visually inspected and assigned a quality code based on the number and quality of absorption lines. Spectra with at least two spectral features (even if one of them is marginal) are considered to have secure redshift measurements. A heliocentric correction is applied to the measured radial velocities based on the sky position of the mask and the date and time of the observation. The heliocentric velocities are not corrected for the changing component of solar motion across our fields; our innermost and outermost fields are separated by  $1.5^\circ$  along the southeastern minor axis, which corresponds to only a  $1.6 \text{ km s}^{-1}$  velocity change.

Spectra in field a0 were reduced using the original reduction techniques briefly outlined above. Detailed discussions of the spectral reduction techniques, quality determination, and S/N measurements used in our survey can be found in Guhathakurta et al. (2006) and Gilbert et al. (2006); the typical velocity error in this field is  $15 \text{ km s}^{-1}$ . Our cross-correlation procedure has since been improved and is described below. An offset of  $+20 \text{ km s}^{-1}$  has been applied to the a0 data to make them consistent with the results of this new cross-correlation procedure.

Spectra in the remainder of the fields were reduced using several improvements to the reduction pipeline. A greater number of stellar templates are used for the spectral cross-correlation, and the template library has been expanded to include spectral templates from the Keck II telescope's Echelle Spectrograph and Imager (ESI) and DEIMOS in addition to the existing Sloan Digital Sky Survey (SDSS) spectral templates. The ESI and DEIMOS templates were included because they more closely match the resolution of the observed spectra. The position of the atmospheric A-band in the observed spectrum is used to correct the observed radial velocity for imperfect centering of the star in the slit (Simon & Geha 2007, in prep; Sohn et al. 2007). The improvement to the spectral templates and the A-band correction allows us to reduce our velocity measurement errors relative to our previous reductions. The median velocity error for the data presented in this paper is  $4.6 \text{ km s}^{-1}$ , estimated from the cross-correlation output routine and confirmed

by repeat measurements of individual stars on overlapping DEIMOS masks.

Spectroscopic data in fields H11 and a0 have been presented in previous papers (Kalirai et al. 2006a; Brown et al. 2003, 2006a). The radial velocity sample for H11 presented in this paper contains  $\approx 50\%$  more M31 RGB stars than the previously published sample, due to the recent recovery of spectra from two CCDs that were not included in these earlier papers and the improvements in the data reduction process described above.

## 3. SELECTING A SAMPLE OF M31 RED GIANTS

The largest source of contaminants in our spectroscopic survey are foreground MW dwarf stars. Background galaxies are easy to identify and remove from the sample on the basis of their spectra and redshifts. However, the radial velocity distribution of MW dwarf stars overlaps that of M31 RGB stars, making identifying individual stars as M31 red giants or MW dwarfs problematic. We use the diagnostic method detailed in Gilbert et al. (2006) to separate M31 RGB stars from MW dwarf star contaminants. The method uses empirical probability distribution functions to estimate the likelihood a given star is an M31 red giant based on five photometric and spectroscopic diagnostics:

- The radial velocity of the star.
- Photometry in the  $M$ ,  $T_2$ , and (surface-gravity sensitive) DDO51 bands
- The measured equivalent width of the Na I doublet at  $8190 \text{ \AA}$  combined with the  $(V - I)_0$  color of the star.
- The position of the star in an  $(I, V - I)$  color magnitude diagram with respect to theoretical RGB isochrones.
- A comparison of the star's photometric vs. spectroscopic metallicity estimates.

The DDO51 diagnostic is only used for field a0, which is the only field in the present work for which DDO51 photometry is available (§ 2.1). The likelihoods for each diagnostic are combined in a weighted average for each star to determine the overall likelihood,  $\langle L_i \rangle$ , the star is an M31 RGB or MW dwarf star (§ A.1). Based on the overall likelihood, each star is identified as either a secure M31 RGB star ( $\langle L_i \rangle > 0.5$ , or  $> 3\times$  more likely to be an M31 RGB star than an MW dwarf) or secure MW dwarf star ( $\langle L_i \rangle < -0.5$ ), or a marginal M31 RGB star ( $0 < \langle L_i \rangle < 0.5$ ) or marginal MW dwarf star ( $-0.5 < \langle L_i \rangle < 0$ ).

An advantage of the diagnostic method for the present analysis is the ability to select a sample that is chosen independently of radial velocity. Since radial velocity is only one of a number of diagnostics which are used to determine the nature of an individual star, the likelihood method (even with the inclusion of the radial velocity diagnostic) presents a significant improvement over the use of velocity cuts to select samples for kinematical analysis by reducing the sensitivity of the sample to velocity. However, by using the likelihood method *without* the radial velocity diagnostic (resulting in overall likelihoods

<sup>15</sup> <http://astron.berkeley.edu/~cooper/deep/spec2d/primer.html>, <http://astron.berkeley.edu/~cooper/deep/spec1d/primer.html>

TABLE 1  
 DETAILS OF SPECTROSCOPIC OBSERVATIONS AND BASIC RESULTS.

Mask	Projected Radius (kpc)	Pointing center:		PA (°E of N)	Date of Obs. (UT)	# Sci. targets <sup>a</sup>	# of M31 Stars <sup>a,b</sup>
		$\alpha_{J2000}$ (h,m,s)	$\delta_{J2000}$ (°,′,″)				
f109_1	9	00:45:46.75	+40:56:53.8	23.90	2005 Aug 29	208	169
H11_1	12	00:46:21.02	+40:41:31.3	21.0	2004 Sep 20	139	89
H11_2	12	00:46:21.02	+40:41:31.3	-21.0	2004 Sep 20	138	88
f116_1	13	00:46:54.53	+40:41:29.5	22.60	2005 Aug 28	199	149
f115_1	15	00:47:32.71	+40:42:00.9	-20.0	2005 Aug 28	191	114
f123_1	18	00:48:05.57	+40:27:16.3	-20.0	2005 Aug 28	171	104
f135_1	18	00:46:24.88	+40:11:35.5	-27.0	2005 Aug 29	146	99
f130_1	22	00:49:11.97	+40:11:45.3	-20.0	2005 Aug 28	108	52
f130_2	23	00:49:37.49	+40:16:07.0	90.0	2006 Nov 21	115	43
f130_3	20	00:48:34.59	+40:16:07.0	90.0	2006 Nov 22	124	41
a0_1	31	00:51:51.32	+39:50:21.4	-17.9	2002 Aug 16	89	25
a0_2	31	00:51:29.59	+39:44:00.8	90.0	2002 Oct 12	89	32
a0_3	29	00:51:50.46	+40:07:00.9	0.0	2004 Jun 17	90	26

<sup>a</sup> A number of targets were observed on two different masks. Therefore, the total number of unique science targets/M31 RGB stars in fields H11, f130 and a0 is less than the reported number. There are 18 M31 RGB stars with duplicate observations (2 in H11, 8 in f130, and 8 in a0), thus the total number of unique M31 RGB stars is 1013.

<sup>b</sup> The number of M31 RGB stars is defined as the number of stars that are identified as secure and marginal M31 RGB stars by the Gilbert et al. (2006) diagnostic method, without the use of the radial velocity diagnostic ( $\langle L_i \rangle_{\psi} > 0$ , § 3).

$\langle L_i \rangle_{\psi}$ ), we are able to select a sample of M31 red giants that is completely *independent* of the radial velocities of the stars.

Fig. 3 presents the radial velocity distribution of stars selected as M31 red giants based on the diagnostic method with (*shaded histograms*) and without (*thick open histograms*) radial velocity included, for multiple  $\langle L_i \rangle$  and  $\langle L_i \rangle_{\psi}$  thresholds. For reference, the radial velocity distribution of all stars with successful velocity measurements is also shown (*thin open histograms*); the MW dwarf star contaminants form the secondary peak centered at  $v_{\text{hel}} \approx -50$  km s<sup>-1</sup>. The M31 RGB distributions are similar, with the sample that includes the radial velocity diagnostic showing a systematic deficiency of stars at radial velocities near 0 km s<sup>-1</sup>. The effect of the radial velocity diagnostic on the overall likelihood ( $\langle L_i \rangle$  and  $\langle L_i \rangle_{\psi}$ ) distributions is discussed in § A.1.

The M31 RGB samples identified by their  $\langle L_i \rangle$  values have a minimal amount of MW dwarf star contamination, but are also kinematically biased against stars with velocities near 0 km s<sup>-1</sup> (§ A.1). The M31 RGB samples identified by their  $\langle L_i \rangle_{\psi}$  values have a slightly larger amount of dwarf contamination (particularly evident in the bottom panel of Figure 3), but the underlying M31 RGB population is kinematically unbiased.

The RGB sample used in this paper is defined as stars that are designated as secure and marginal M31 red giants by the diagnostic method, with the radial velocity likelihood *not* included in the calculation of a star’s overall likelihood of being an M31 RGB star (i.e.,  $\langle L_i \rangle_{\psi} > 0$ ). The number of M31 RGB stars in each field is listed in Table 1. The  $\langle L_i \rangle_{\psi} > 0$  threshold maximizes the completeness of the underlying, *kinematically unbiased* M31 RGB population, but introduces an overall MW dwarf star contamination of 5% to the sample (§ A.2). The contamination is largely constrained to  $v_{\text{hel}} > -150$  km s<sup>-1</sup> due to the velocity distribution of MW dwarf stars, and its effect on the measured parameters of the M31 RGB

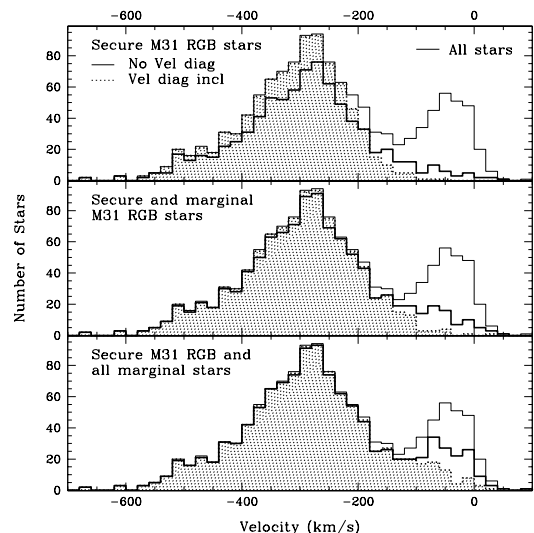


FIG. 3.— The radial velocity distributions of samples with (*shaded/dotted histograms*) and without (*thick open histograms*) the radial velocity diagnostic included in the overall likelihood calculation. The radial velocity distribution of all stars with successful radial velocity measurements is shown for comparison (*thin open histograms*); the MW dwarf star contaminants form the peak at  $v_{\text{hel}} \approx -50$  km s<sup>-1</sup>. *Top*: Stars designated as secure ( $[\langle L_i \rangle, \langle L_i \rangle_{\psi}] > 0.5$ ) M31 red giants only. *Middle*: Stars designated as marginal and secure M31 red giants ( $[\langle L_i \rangle, \langle L_i \rangle_{\psi}] > 0$ ). *Bottom*: Stars designated as marginal MW dwarfs, marginal M31 red giants, and secure M31 red giants ( $[\langle L_i \rangle, \langle L_i \rangle_{\psi}] > -0.5$ ). The distributions are similar, but there is a deficiency of stars at velocities near 0 km s<sup>-1</sup> in the sample that includes radial velocity as a diagnostic.

sample is quantified in § A.3.

#### 4. STELLAR KINEMATICS IN M31’S SOUTHEAST MINOR-AXIS FIELDS

The data presented in this paper span a range in projected radial distance from the center of M31 of 9 to

30 kpc, along the southeastern minor axis. We refer to this region as the “inner spheroid,” even though it has traditionally been referred to as the “halo” of M31. This region departs from the classical picture of a stellar halo formed from observations of the Milky Way: M31’s inner spheroid is about  $10\times$  more metal-rich than the MW’s halo (Mould & Kristian 1986; Durrell et al. 2004) and follows a de Vaucouleurs  $r^{1/4}$  surface density profile (Pritchet & van den Bergh 1994; Durrell et al. 2004), while the surface density profile of the MW halo follows an  $r^{-2}$  power law. In other words, M31’s inner spheroid appears to be a continuation of its central bulge. Recent observations have discovered an outer stellar “halo” in M31 which is relatively metal-poor (Kalirai et al. 2006b; Chapman et al. 2006), has a surface density profile that follows an  $\sim r^{-2}$  power law (Guhathakurta et al. 2005; Irwin et al. 2005), and has been detected out to  $R_{\text{proj}} = 165$  kpc (Gilbert et al. 2006).

These observations imply that the spheroid of M31 has two components: an inner, de Vaucouleurs profile spheroid, and an outer, power-law profile halo. We thus use the term *inner spheroid* to distinguish the region  $R_{\text{proj}} \sim 9\text{--}30$  kpc from the canonical central bulge and the newly discovered stellar halo of M31. The outer limit of this region is well-defined; a break in the surface brightness profile of M31 RGB stars has been observed at  $R_{\text{proj}} \sim 20\text{--}30$  kpc (Guhathakurta et al. 2005; Irwin et al. 2005), and there is observational evidence that the crossover between the predominantly metal-rich population of the inner spheroid and the predominantly metal-poor population of the outer halo occurs at  $R_{\text{proj}} \sim 30$  kpc (Kalirai et al. 2006b). The inner limit of this region is arbitrary, as the relationship between this component and the central bulge of M31 is not yet clear.

The rest of this section characterizes the line of sight velocity distribution of stars in the inner spheroid of M31 through maximum-likelihood fits of Gaussians to the combined data set (§ 4.1) and to individual fields (§ 4.2). Gaussians provide a convenient means of fitting for multiple kinematical components in the data and characterizing their mean velocity and velocity dispersion. The true shape of the velocity distribution of a structural component in M31 is likely to be different from a pure Gaussian. However, given the limited sample size and the absence of any specific physical model, the choice of Gaussians seems appropriate.

#### 4.1. Maximum-Likelihood Fits to the Velocity Distribution of the Combined Data Set

Figure 4 shows the combined radial velocity distribution of M31 RGB stars from all eight fields along the minor axis, ranging from 9 to 30 kpc in projected radial distance from the center of M31. Fits to the radial velocity distribution were made using a maximum-likelihood technique; the best-fit single (a) and double (b) Gaussians are displayed in Figure 4. A reduced  $\chi^2$  analysis rules out the single-Gaussian fit, as the probability is  $\ll 1\%$  that the observed radial velocities were drawn from the best-fit distribution. The observed velocity distribution is well fit by a sum of two Gaussians (solid curve, panel b of Fig. 4), composed of a wide Gaussian (dashed curve) centered at  $\langle v \rangle^{\text{sph}} = -287.2_{-7.7}^{+8.0}$  km s $^{-1}$ , with a

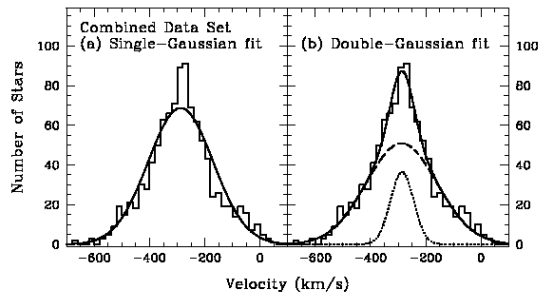


FIG. 4.— The radial velocity distribution of the M31 RGB inner spheroid population. A maximum-likelihood analysis was used to fit an analytic function to the distribution. (a) The best fit single Gaussian has parameters  $\langle v \rangle^{\text{sph}} = -287$  km s $^{-1}$  and  $\sigma_v^{\text{sph}} = 117$  km s $^{-1}$ . A  $\chi_{\text{red}}^2$  test rules out the single-Gaussian fit at a very high confidence level. (b) The best constrained double-Gaussian fit (Table 2) is shown as a solid curve, with the narrow component and wide components displayed separately as dotted and dashed curves, respectively.

width of  $\sigma_v^{\text{sph}} = 128.9_{-6.9}^{+7.7}$  km s $^{-1}$ , and a narrow Gaussian (dotted curve) centered at  $\langle v \rangle^{\text{sub}} = -285.4_{-12.4}^{+12.8}$  km s $^{-1}$  with a width of  $\sigma_v^{\text{sub}} = 42.2_{-14.3}^{+12.5}$  km s $^{-1}$ , which comprises  $19_{-8}^{+9}\%$  of the total population (quoted errors represent the 90% confidence limits from the maximum-likelihood analysis). Due to the MW dwarf star contaminants in the M31 RGB sample (§ 3), the true  $\langle v \rangle^{\text{sph}}$  value of the wide Gaussian component is 15 to 20 km s $^{-1}$  more negative than the best-fit value (§ A.3), making it consistent with the systemic velocity of M31 ( $v_{\text{sys}} = -300$  km s $^{-1}$ ). The kinematically hot component corresponds to the inner spheroid of M31 (quantities related to this component are denoted with the subscript “sph”), while the kinematically cold component corresponds to substructure in the inner spheroid (denoted with the subscript “sub”); the discussion of these components and their properties will be deferred to § 5 and § 6, respectively. The wider of the two Gaussian components in the double Gaussian fit to the combined data set is hereafter referred to as  $G^{\text{sph}}(v)$ .

Figure 5 shows error estimates from the maximum-likelihood analysis (in the form of  $\Delta\chi^2 \equiv \chi^2 - \chi_{\text{min}}^2$  curves) for the five double-Gaussian parameters. The best-fit value of each parameter is marked as well as the 90% confidence limits. The  $\Delta\chi^2$  curves have a deep minimum for all five parameters, an indication that the double-Gaussian model is a good description of the observed radial velocity distribution of inner spheroid stars.

#### 4.2. Maximum-Likelihood Fits to the Velocity Distributions of Individual Fields

As discussed in the previous section, the combined data set shows definite evidence of a kinematically cold component centered at about  $-300$  km s $^{-1}$  that comprises a significant fraction (19%) of the total population. We next investigate which of the fields in our data set are the main contributors to this cold population. Figure 6 shows velocity histograms for each of the eight fields analyzed in this paper. While most of the fields display hints of substructure—in the form of one or more small possible peaks in their velocity distribution that may be marginally significant relative to the (substantial) Poisson noise—we are specifically interested in

TABLE 2  
 RADIAL VELOCITY DISTRIBUTIONS: BEST FIT GAUSSIAN PARAMETERS.

Field	Best fit Gaussian Parameters <sup>a</sup>				Fraction $N_{\text{sub}}/N_{\text{tot}}$
	Cold Component		Hot Spheroid <sup>b</sup>		
	$\langle v \rangle^{\text{sub}}$	$\sigma_v^{\text{sub}}$	$\langle v \rangle^{\text{sph}}$	$\sigma_v^{\text{sph}}$	
All fields	$-285.4_{-12.4}^{+12.8}$	$42.2_{-14.3}^{+12.5}$	$-287.2_{-7.7}^{+8.0}$	$128.9_{-6.9}^{+7.7}$	$0.19_{-0.08}^{+0.09}$
f109	...	...	$-274.5_{-15.3}^{+15.4}$	$120.7_{-10.1}^{+11.7}$	...
H11	$-294.3_{-17.6}^{+17.3}$	$55.5_{-12.7}^{+15.6}$	$-287.2$	$128.9$	$0.44_{-0.16}^{+0.16}$
f116	$-309.4_{-17.5}^{+19.2}$	$51.2_{-15.0}^{+24.4}$	$-287.2$	$128.9$	$0.44_{-0.17}^{+0.22}$
f115	...	...	$-270.9_{-18.6}^{+18.6}$	$120.1_{-12.0}^{+14.4}$	...
f123	$-279.4_{-4.6}^{+5.1}$	<sup>c</sup> $10.6_{-5.0}^{+6.9}$	$-287.2$	$128.9$	$0.31_{-0.11}^{+0.11}$
f135	...	...	$-315.1_{-21.3}^{+21.3}$	$127.8_{-13.6}^{+16.5}$	...
f130	...	...	$-259.8_{-19.2}^{+19.3}$	$131.5_{-12.5}^{+14.8}$	...
a0	...	...	$-299.2_{-25.2}^{+25.2}$	$131.5_{-21.6}^{+29.5}$	...

<sup>a</sup> A double Gaussian fit is presented for the combined sample, as it is a poor fit to a single Gaussian (§ 4.1). Constrained double Gaussian fits are presented for three of the fields (H11, f116, and f123), with the wider component held fixed (adopting the fit to the combined sample). Single Gaussian fits are presented for the remaining five fields. The reader is referred to § 4.2 for details of the fits to individual fields. Errors quoted represent the 90% confidence limits from the maximum-likelihood analysis.

<sup>b</sup> The M31 RGB sample used in this analysis was chosen to ensure a high degree of completeness, and thus suffers from some MW dwarf contamination (§ A.2). The MW dwarf star contaminants are largely at  $v_{\text{hel}} > -150 \text{ km s}^{-1}$ , and cause the best-fit  $\langle v \rangle^{\text{sph}}$  values to be biased towards more positive velocities. The true  $\langle v \rangle^{\text{sph}}$  values of the M31 RGB population are 15 to 20  $\text{km s}^{-1}$  more negative than listed here. The effect on  $\sigma_v^{\text{sph}}$  is negligible (§ A.3).

<sup>c</sup> The median velocity error for the stars in f123 is 4.6  $\text{km s}^{-1}$ . The estimated intrinsic velocity dispersion of the cold component in f123 after accounting for velocity measurement error is 9.5  $\text{km s}^{-1}$ .

judging each field’s contribution to the cold component at  $\sim -300 \text{ km s}^{-1}$ . For this purpose, we compare the data in each field to three sets of Gaussian fits. We describe each of the fits below, summarize the results of the fits, and then list the quantitative details of the fits for each field.

First, the radial velocity distribution in each field is compared to the Gaussian  $G^{\text{sph}}(v)$  defined by  $\langle v \rangle^{\text{sph}} = -287.2 \text{ km s}^{-1}$ ,  $\sigma_v^{\text{sph}} = 128.9 \text{ km s}^{-1}$  (§ 4.1) using the reduced  $\chi^2$  statistic ( $\chi_{\text{red}}^2$ ). Fields f109, f115, and a0 are consistent with being drawn from  $G^{\text{sph}}(v)$ , and so are ruled out as significant contributors to the  $\sim -300 \text{ km s}^{-1}$  cold component. The rest of the fields are at least marginally inconsistent with being drawn from  $G^{\text{sph}}(v)$ .

Second, a maximum-likelihood single-Gaussian fit is performed on the radial velocity distribution in each field and compared to the data. Fields f123 and f135 are inconsistent with their respective best-fit single Gaussians (based on the  $\chi_{\text{red}}^2$  statistic) and are therefore suspected to contain substructure. The remaining fields (f109, H11, f116, f115, f130, and a0) are consistent with their best-fit single Gaussians. For fields f109, f115, f130, and a0, the best-fit Gaussians are consistent with  $G^{\text{sph}}(v)$ , and they are thus ruled out as significant contributors to the  $\sim -300 \text{ km s}^{-1}$  cold component. Fields f116 and H11 are suspected to contain substructure because their best-fit Gaussians are significantly narrower than  $G^{\text{sph}}(v)$ . Previous kinematic studies of M31’s inner spheroid, including this one, have found a ubiquitously broad distribution of radial velocities ( $v_{\text{hel}} \approx 0$  to  $\approx -600 \text{ km s}^{-1}$ ;

§ 5). Thus, the anomalously narrow single Gaussian fits in fields f116 and H11 cause us to suspect them of being contributors to the  $\sim -300 \text{ km s}^{-1}$  cold component.

Third, we carry out a maximum-likelihood fit to all fields using a constrained double Gaussian, with  $G^{\text{sph}}(v)$  as the fixed wide Gaussian component. Fields H11, f116, and f123 are well fit by a constrained double Gaussian (based on the  $\chi_{\text{red}}^2$  statistic and well-defined minima for the variable Gaussian parameters). These three fields are significant contributors to the  $\sim -300 \text{ km s}^{-1}$  cold component, and the constrained double-Gaussian fit is adopted as the preferred fit in the subsequent discussion. The best-fit cold component in the constrained double-Gaussian fit to f130 is centered at  $\sim -50 \text{ km s}^{-1}$ , but this likely represents residual contamination by MW dwarf stars (§ 3, § A). The remaining fields (f109, f115, f135, and a0) are poor fits to a constrained double-Gaussian in that the Gaussian parameters do not have well-defined minima.

In summary:

- Three fields, H11, f116, and f123 are identified as significant contributors to the  $\sim -300 \text{ km s}^{-1}$  cold component.
- Although field f135 shows evidence of substructure, it is a poor fit to a constrained double-Gaussian and is not a definite contributor to the  $\sim -300 \text{ km s}^{-1}$  cold component. (However, the fit may be confused by the presence of multiple cold components; § 7.1.3.)
- Four fields, f109, f115, f130, and a0, are not sig-

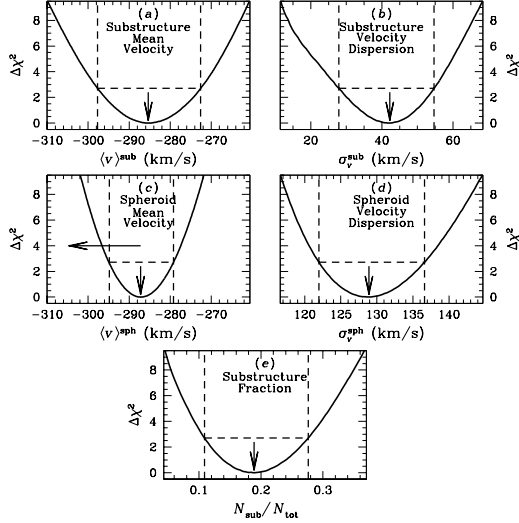


FIG. 5.— Results of the maximum-likelihood analysis for the double-Gaussian fit to the combined M31 RGB inner spheroid sample. The optimal value of each parameter is marked with an arrow, and the 90% confidence limits from the maximum-likelihood analysis are marked with dashed lines. The upper limit of the y-axis represents the 99% confidence limits. The parameter  $\Delta\chi^2 \equiv \chi^2 - \chi^2_{\min}$  is plotted as a function of (a) mean velocity of the cold substructure component (narrow Gaussian),  $\langle v \rangle^{\text{sub}}$ , (b) velocity dispersion of the cold component,  $\sigma_v^{\text{sub}}$ , (c) mean velocity of the M31 inner spheroid (wide Gaussian),  $\langle v \rangle^{\text{sph}}$ , (d) velocity dispersion of the M31 inner spheroid,  $\sigma_v^{\text{sph}}$ , and (e) fraction of the total M31 RGB population in the cold component,  $N_{\text{sub}}/N_{\text{tot}}$ . The horizontal arrow in panel (c) represents the correction to the  $\langle v \rangle^{\text{sph}}$  value necessary to offset the bias caused by MW dwarf contamination at  $v_{\text{hel}} > -150 \text{ km s}^{-1}$  (§ A.3).

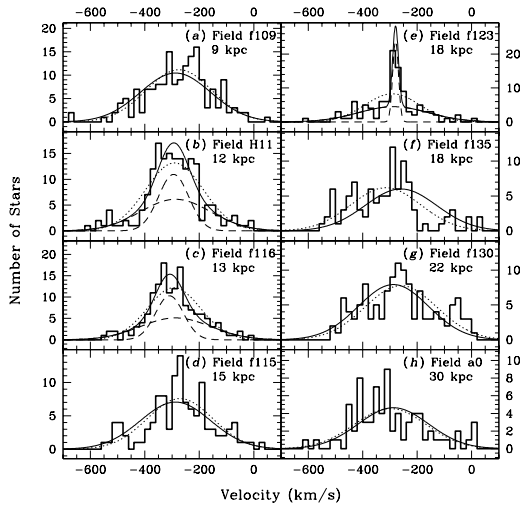


FIG. 6.— Velocity histograms for each of the individual fields with best-fit Gaussians overlaid. Fields that did not show clear evidence of substructure (f109, f115, f130, f135 and a0, § 4.2) are shown with the Gaussian component from the double-Gaussian fit to the full sample ( $G^{\text{sph}}(v)$ , solid curves), as well as the best-fit single Gaussian to the individual field (dotted curves). Fields with evidence of substructure (H11, f116, f123), are shown with both their best-fit single (dotted curves) and double (solid curves) Gaussians. For the constrained double-Gaussian fits, both the narrow and broad ( $G^{\text{sph}}(v)$ ) Gaussian components are shown (dashed curves) scaled to their relative contributions.

nificant contributors to the  $\sim -300 \text{ km s}^{-1}$  cold component.

Each field is discussed individually below, and Table 2 summarizes the preferred fits (single or double-Gaussian) to the velocity distributions in each field.

*Field f109:* The data in this field are consistent with being drawn from the Gaussian  $G^{\text{sph}}(v)$  (§ 4.1). The best-fit single Gaussian to the data in this field has parameters  $\langle v \rangle = -274.5 \text{ km s}^{-1}$  and  $\sigma = 120.7 \text{ km s}^{-1}$ , and the data are also consistent with being drawn from this distribution.

*Field H11:* The probability the data in this field are drawn from the Gaussian  $G^{\text{sph}}(v)$  is  $P < 1\%$ , thus the data are inconsistent with this distribution. The best-fit single Gaussian to the data in this field has parameters  $\langle v \rangle = -291.1 \pm 11.6 \text{ km s}^{-1}$  and  $\sigma = 106.2^{+8.7}_{-7.7} \text{ km s}^{-1}$ , and the data are consistent with being drawn from this distribution. However, the best-fit value of  $\sigma$  in this field is anomalously low compared to the value of  $\sigma_v^{\text{sph}}$  determined from the double-Gaussian fit to the combined data set: the two values are inconsistent at the  $\sim 3.5\sigma$  level. This suggests that there is a kinematically cold population in this field, and a comparison of the data to the constrained double-Gaussian fit to this field ( $\langle v \rangle^{\text{sub}} = -294.3 \text{ km s}^{-1}$ ,  $\sigma_v^{\text{sub}} = 55.5 \text{ km s}^{-1}$ ,  $N_{\text{sub}}/N_{\text{tot}} = 0.44$ ) returns a  $\chi^2_{\text{red}}$  that is significantly smaller than the  $\chi^2_{\text{red}}$  of the single Gaussian fit.

*Field f116:* The data in this field are inconsistent with being drawn from the Gaussian  $G^{\text{sph}}(v)$ . The best-fit single Gaussian to the data in this field has parameters  $\langle v \rangle = -292.9^{+11.5}_{-11.6} \text{ km s}^{-1}$  and  $\sigma = 97^{+8.7}_{-7.5} \text{ km s}^{-1}$ , and the data are consistent with being drawn from this distribution. As in field H11, the best-fit value of  $\sigma$  is inconsistent with  $\sigma_v^{\text{sph}}$  from the combined data set, at the  $\sim 4.2\sigma$  level. A comparison of the data to the constrained double-Gaussian fit to this field ( $\langle v \rangle^{\text{sub}} = -309.4 \text{ km s}^{-1}$ ,  $\sigma_v^{\text{sub}} = 51.2 \text{ km s}^{-1}$ ,  $N_{\text{sub}}/N_{\text{tot}} = 0.44$ ) returns a significantly smaller  $\chi^2_{\text{red}}$  than that of the single-Gaussian fit.

*Field f115:* The data in this field are consistent with being drawn from the Gaussian  $G^{\text{sph}}(v)$ , as well as the best-fit single Gaussian ( $\langle v \rangle^{\text{sph}} = -270.9 \text{ km s}^{-1}$ ,  $\sigma_v^{\text{sph}} = 120.1 \text{ km s}^{-1}$ ).

*Field f123:* The probability that the data in this field are drawn from the Gaussian  $G^{\text{sph}}(v)$  is  $P \ll 1\%$ . The probability that the data are drawn from the best-fit single Gaussian ( $\langle v \rangle^{\text{sph}} = -270.9 \text{ km s}^{-1}$ ,  $\sigma_v^{\text{sph}} = 120.1 \text{ km s}^{-1}$ ) in this field is also  $\ll 1\%$ . The data in this field are strongly inconsistent with being drawn from any single Gaussian, but they are consistent with the constrained double-Gaussian fit ( $\langle v \rangle^{\text{sub}} = -279.4 \text{ km s}^{-1}$ ,  $\sigma_v^{\text{sub}} = 10.6 \text{ km s}^{-1}$ ,  $N_{\text{sub}}/N_{\text{tot}} = 0.31$ ). The median velocity error for the stars in field f123 is  $4.6 \text{ km s}^{-1}$ , therefore the intrinsic velocity dispersion of the cold component in this field is estimated to be  $9.5 \text{ km s}^{-1}$ .

*Field f135:* The data in this field are inconsistent with being drawn from the Gaussian  $G^{\text{sph}}(v)$  ( $P \sim 1\%$ ). The best-fit single Gaussian to the data in this field has parameters  $\langle v \rangle^{\text{sph}} = -315.1 \text{ km s}^{-1}$  and  $\sigma_v^{\text{sph}} = 127.8 \text{ km s}^{-1}$ , but the data are also inconsistent with being drawn from this distribution ( $P \lesssim 1\%$ ). However, the maximum-likelihood analysis was unable to constrain a double-Gaussian fit to any reasonable degree



of certainty— i.e., the error estimates on the parameters show no strong global minima. Field f135 is therefore treated as a field without a *definite* detection of substructure, although in § 7.1.3 we discuss the possible presence of multiple kinematically-cold components in this field.

*Field f130:* The data in this field are inconsistent with being drawn from the Gaussian  $G^{\text{sph}}(v)$  ( $P \lesssim 1\%$ ), but are consistent with being drawn from the best-fit single Gaussian ( $\langle v \rangle^{\text{sph}} = -259.8 \text{ km s}^{-1}$ ,  $\sigma_v^{\text{sph}} = 131.5 \text{ km s}^{-1}$ ). The best-fit single Gaussian for this field has parameters which are consistent with  $G^{\text{sph}}(v)$  (Table 2).

*Field a0:* The data in this field are consistent with being drawn from the Gaussian  $G^{\text{sph}}(v)$  as well as the best-fit single Gaussian ( $\langle v \rangle^{\text{sph}} = -299.2 \text{ km s}^{-1}$ ,  $\sigma_v^{\text{sph}} = 131.5 \text{ km s}^{-1}$ ).

We now have a characterization of the kinematical properties of the combined data set and the individual fields, and have identified the fields which significantly contribute to the  $\sim -300 \text{ km s}^{-1}$  cold component discovered in the combined data set (H11, f116, and f123). The number of stars in fields H11, f116, and f123 which are associated with the cold component comprise 17% of the total number of M31 RGB stars in the sample, confirming that these fields are the primary contributors to the cold component. Next, we discuss the trends in the properties of the dynamically hot and cold populations (§ 5 and § 6, respectively), followed by possible physical interpretations of the cold component (§ 7).

## 5. VELOCITY DISPERSION OF M31'S VIRIALIZED INNER SPHEROID

As discussed in § 4, the radial velocity distribution of the combined data set contains a significant cold component at  $v_{\text{hel}} \sim -300 \text{ km s}^{-1}$ . An analysis of the kinematical profile of the individual fields shows that this is due to the presence of a significant amount of substructure in three of the fields (§ 4.2). The kinematically hot component in the double Gaussian fit to the combined data set presumably represents the underlying virialized inner spheroid of M31. The velocity dispersion of the spheroid based on a maximum-likelihood double Gaussian fit to the combined data set (1013 M31 RGB stars) is  $\sigma_v^{\text{sph}} = 128.9 \text{ km s}^{-1}$ .

We have combined all of the fields to get a more robust estimate of the velocity dispersion of the inner spheroid, since the individual fields suffer from small number statistics. However, the dynamical quantities ( $\langle v \rangle^{\text{sph}}$ ,  $\sigma_v^{\text{sph}}$ ) may have radial dependencies. The velocity dispersion of spheroids is expected to decrease with increasing radius (e.g., Navarro et al. 1996, 2004; Mamon & Lokas 2005; Dekel et al. 2005). Rotation of the spheroid or the tangential motion of M31 could result in a radial dependency of  $\langle v \rangle^{\text{sph}}$ , but since our fields are mostly aligned along the minor axis and cover a relatively small radial range, we do not expect to be sensitive to these effects.

To test for a dependency of the dynamical quantities on radius, we analyze the single Gaussian fits to the velocity distributions in each of the five fields which do not show clear evidence of substructure as described in § 4.2 (Table 2). The  $\Delta\chi^2$  error estimates for the best-fit single Gaussian parameters in these fields are shown

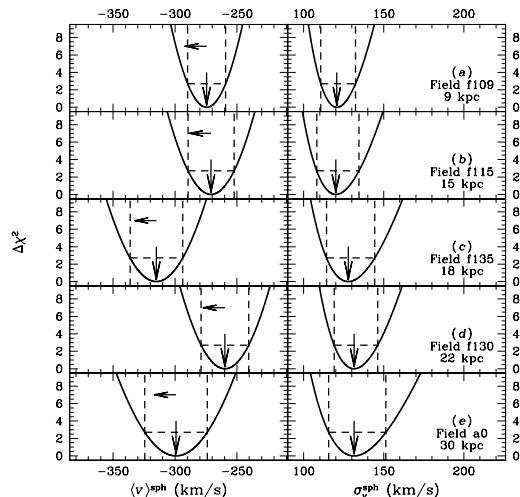


FIG. 7.— Results of the maximum-likelihood analysis for the single-Gaussian fits to individual fields that do not show clear evidence of the  $\sim -300 \text{ km s}^{-1}$  cold component in their radial velocity distributions (§ 4.2). The panels show  $\Delta\chi^2$  for the mean velocity  $\langle v \rangle^{\text{sph}}$  (left) and velocity dispersion  $\sigma_v^{\text{sph}}$  (right) of M31 RGB stars in fields (a) f109, (b) f115, (c) f135, (d) f130, and (e) a0. As in Figure 5, the optimal values of  $\langle v \rangle^{\text{sph}}$  and  $\sigma_v^{\text{sph}}$  are marked by arrows, and the 90% confidence limits are shown as dashed lines. The horizontal arrow in each of the left panels represents the correction (magnitude and direction) to the  $\langle v \rangle^{\text{sph}}$  value necessary to offset the bias caused by MW dwarf contamination at  $v_{\text{hel}} > -150 \text{ km s}^{-1}$  (§ A.3).

in Figure 7. The best-fit  $\langle v \rangle^{\text{sph}}$  values in each field are largely consistent with the systemic velocity of M31 ( $v_{\text{sys}} = -300 \text{ km s}^{-1}$ ) once the effect of MW dwarf star contamination is taken into account, with the exception of f135, whose  $\langle v \rangle^{\text{sph}}$  is significantly more negative. Our data show no evidence for a decreasing  $\sigma_v^{\text{sph}}$  with increasing radius. However, the fields discussed in this paper only span a range in projected radial distance of  $R_{\text{proj}} \sim 9$  to 30 kpc. This is small compared to the size of the total M31 spheroid (inner spheroid and outer halo), which has been shown to extend to 165 kpc (Gilbert et al. 2006). Battaglia et al. (2005) use a sample of 240 Galactic halo objects to determine the radial velocity dispersion of the Milky Way halo, and find that it has an almost constant value of  $120 \text{ km s}^{-1}$  out to 30 kpc, beyond which it decreases with increasing radial distance, declining to  $50 \text{ km s}^{-1}$  at 120 kpc.

There have been a few previous measurements of the velocity dispersion based on M31 spheroid stars. The closest analog to the present study is Reitzel & Guhathakurta (2002), who fit 80 candidate M31 RGB stars at  $R_{\text{proj}} = 19 \text{ kpc}$  on the southeastern minor axis with a combination of the Galactic standard model and a wide Gaussian. They found  $\sigma_v^{\text{sph}} \sim 150 \text{ km s}^{-1}$  for the M31 velocity dispersion, with the number of M31 RGB stars estimated to be 43% of the population. Guhathakurta et al. (2006) studied a field on the giant southern stream at  $R_{\text{proj}} = 33 \text{ kpc}$  and found a velocity dispersion of  $\sigma_v^{\text{sph}} = 65_{-21}^{+32} \text{ km s}^{-1}$  for the underlying spheroid based on a sample of  $\approx 21$  stars. However, if 3 likely RGB stars with  $v_{\text{hel}} > -150 \text{ km s}^{-1}$  are included, the estimated velocity dispersion in this field increases to

$$\sigma_v^{\text{sph}} = 116_{-22}^{+31} \text{ km s}^{-1}.$$

Chapman et al. (2006) have measured a mean velocity dispersion of  $\sigma_v^{\text{sph}} = 126 \text{ km s}^{-1}$  for the inner spheroid of M31 using  $\sim 800$  RGB stars in multiple fields surrounding M31. They determine that the spheroid has a central velocity dispersion of  $152 \text{ km s}^{-1}$  which decreases by  $-0.9 \text{ km s}^{-1} \text{ kpc}^{-1}$  out to  $R_{\text{proj}} \sim 70 \text{ kpc}$ . Many of their fields are near M31’s major axis and have significant contamination from the extended rotating component identified as the extended disk in Ibata et al. (2005). They isolate a sample of M31 spheroid stars by removing all stars within  $160 \text{ km s}^{-1}$  of the disk velocity in each field, and by removing all stars with  $v_{\text{hel}} > -160 \text{ km s}^{-1}$  (MW dwarf star contaminants). This “windowing” technique leaves them with a sample of M31 spheroid stars that is significantly incomplete, but is largely uncontaminated by M31’s extended disk or MW dwarf stars. Based on the Chapman et al. (2006) result, we would expect to measure a velocity dispersion of  $146 \text{ km s}^{-1}$  in our innermost field, f109, which would decrease to a velocity dispersion of  $125 \text{ km s}^{-1}$  in our outermost field, a0. The predicted velocity dispersion of  $146 \text{ km s}^{-1}$  in field f109 exceeds the 90% confidence limits of the maximum-likelihood fit and is just within the 99% confidence limit, and the data presented in this paper show no evidence of a strong trend in  $\sigma_v^{\text{sph}}$  with radius.

The previous measurements of the stellar velocity dispersion of the M31 spheroid relied either on samples that were chosen on the basis of radial velocity cuts or on a statistical fit to the combined M31 RGB and MW dwarf populations. Our measurement of the velocity dispersion of M31’s spheroid is unique in that it is based on a sample of spectroscopically confirmed M31 RGB stars that were chosen *without* the use of radial velocity (§ 3). Our method also allows us to quantify and correct for the effect of MW dwarf star contamination (§ A.2 and § A.3).

## 6. PROPERTIES OF THE MINOR-AXIS SUBSTRUCTURE

### 6.1. Spatial Trends: Kinematics and Structure

As discussed in § 4.2, fields H11, f116, and f123 show evidence of the cold component at  $\sim -300 \text{ km s}^{-1}$  in their radial velocity distributions (Fig. 6), and are well fit by a sum of two Gaussians with  $G^{\text{sph}}(v)$  as the fixed wide Gaussian component (Table 2). The  $\Delta\chi^2$  error estimates for the free parameters ( $\langle v \rangle^{\text{sub}}$ ,  $\sigma_v^{\text{sub}}$ , and  $N_{\text{sub}}/N_{\text{tot}}$ ) are shown in Figure 8 for each field.

If the three fields are considered together, a pattern emerges. Both the velocity dispersion and the fraction of stars in the cold component decrease with increasing radial distance. The cold component in fields H11 and f116 (at  $R_{\text{proj}} = 12$  and  $13 \text{ kpc}$ , respectively) is significantly wider than the cold component in field f123 ( $R_{\text{proj}} = 18 \text{ kpc}$ ). The cold component also appears to be more dominant by number (surface brightness) over the hot component in fields H11 and f116 than in field f123.

Figure 9 presents the velocities of the M31 RGB stars as a function of their distance along the major and minor axes of M31. The cold component can be seen as a triangular-shaped feature that narrows to a sharp point as the distance along the minor axis increases. The fields

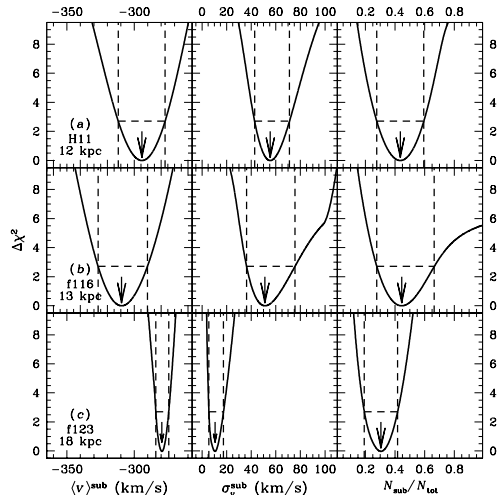


FIG. 8.— Results of the maximum-likelihood analysis for the narrow Gaussian parameters from the constrained double-Gaussian fits to fields (a) H11, (b) f116, and (c) f123. The panels show  $\Delta\chi^2$  as a function of (left) mean velocity  $\langle v \rangle^{\text{sub}}$ , (middle) velocity dispersion  $\sigma_v^{\text{sub}}$ , and (right) fraction of stars in the cold component,  $N_{\text{sub}}/N_{\text{tot}}$ . The parameters of the wide Gaussian component in these fits have been fixed at the values of the Gaussian  $G^{\text{sph}}(v)$  (§ 4.1). As in Figure 5, the optimal values of each parameter are marked by arrows, and the 90% confidence limits are shown as dashed lines. The velocity dispersion decreases with increasing radial distance from the center of M31.

that overlap the triangular-shaped feature in minor axis distance are (in order of increasing distance along the minor axis) H11, f116, f115, f135, and f123. Stars in fields H11, f116 and f123 that are within the area denoted by the dotted line are shown as red crosses in the bottom panel. In the fields in which it is observed, the cold component is spread evenly along the direction of the major axis, and is centered at  $v_{\text{hel}} \sim -285 \text{ km s}^{-1}$ . The majority of the fields overlap in position along the major axis; the exception is field f135, which is the isolated set of points at large major axis distances ( $-0.51^\circ$  to  $-0.36^\circ$ , or  $-7.0 \text{ kpc}$  to  $-4.9 \text{ kpc}$ ) in the bottom panel of Figure 9. Field f123 extends from  $-1.18^\circ$  to  $-1.39^\circ$  ( $16.1 \text{ kpc}$  to  $19.0 \text{ kpc}$ ) along the minor axis; the tip of the feature is seen in this field. This field also has the coldest substructure in the radial velocity histograms (Fig. 6, Table 2). Field H11 brackets the other edge of the feature along the minor axis. Field H11 has a range in minor axis distance of  $-0.78^\circ$  to  $-0.99^\circ$  ( $10.7 \text{ kpc}$  to  $13.5 \text{ kpc}$ ), and has a large degree of overlap with field f116 in both their minor and major axis distance ranges. The fits to the cold component in these two fields return similar  $\sigma_v^{\text{sub}}$  and  $N_{\text{sub}}/N_{\text{tot}}$  estimates (Table 2).

Of the fields in which substructure was not clearly detected kinematically (§ 4.2), fields f135 and f115 are both within the minor axis distance range spanned by the observed substructure (dotted triangular region in upper panel of Fig. 9). A two-sided Kolmogorov-Smirnov (KS) test finds that the radial velocity distribution of field f115 is consistent with the radial velocity distribution of its closest neighbor, field f116 (Fig. 2), although it is inconsistent with the best constrained double Gaussian fit to field f116. Although the radial velocity distribution

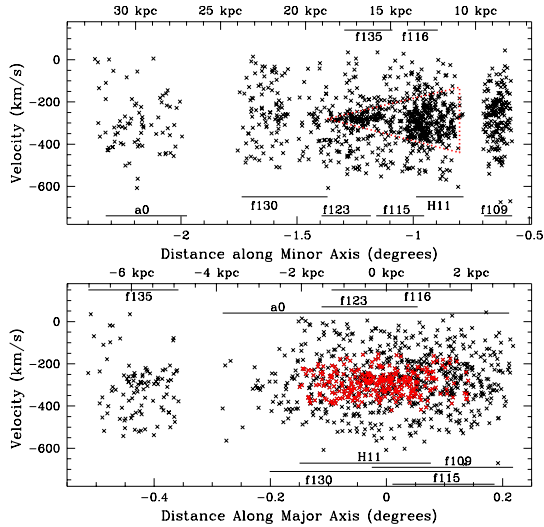


FIG. 9.— Distribution of M31 RGB stars in velocity vs. distance along the minor (*top*) and major (*bottom*) axes of M31. The range of minor (major) axis distances of stars in each field are shown in the top (bottom) panel. *Top*: The cold component is visible as a triangular feature that starts at  $-0.8^\circ$  (10.9 kpc) and narrows to a point at  $-1.35^\circ$  (18.4 kpc) along the minor axis. This feature is outlined in red (*dotted line*). *Bottom*: Stars in fields H11, f116, and f123 that fall within the triangular outline in the top panel are colored red. In the fields in which the  $\sim -300 \text{ km s}^{-1}$  cold component is present, it is spread evenly as a function of projected distance from the minor axis.

of field f135 is not well-fit by a double Gaussian (§ 4.2), there is a concentration of stars near  $v_{\text{hel}} \sim -300 \text{ km s}^{-1}$  in its radial velocity distribution (Fig. 6). We will discuss these fields further in the context of the physical interpretation of the cold substructure (§ 7.1). Fields f130 and a0 are at larger minor axis distances than the tip of the feature, and field f109 is interior to the feature. The fact that substructure is not detected in these fields is consistent with our favored physical interpretation of the  $-300 \text{ km s}^{-1}$  cold component, which will be discussed in § 7.1.

## 6.2. Metallicity Distribution

So far we have considered only the kinematic properties of the minor axis population. The distribution of stellar metallicities, however, is also a powerful diagnostic of the presence and origin of substructure, since different galactic components (e.g., disk, inner spheroid) and tidal debris have different formation histories, and therefore different chemical abundances.

Figure 10(a) displays  $[\text{Fe}/\text{H}]$  vs.  $v_{\text{hel}}$  for the M31 RGB stars. The  $[\text{Fe}/\text{H}]$  values are based on a comparison of the star's position within the  $(I, V - I)$  CMD to a finely spaced grid of theoretical 12 Gyr,  $[\alpha/\text{Fe}] = 0$  stellar isochrones (Kalirai et al. 2006b; Vandenberg et al. 2006) adjusted to the distance of M31 (783 kpc; Stanek & Garnavich 1998; Holland 1998). Stars with  $[\text{Fe}/\text{H}] < -1$  appear to be evenly distributed in velocity, while there is an obvious clump of metal-rich stars with velocities near  $-300 \text{ km s}^{-1}$ . The bottom panels (b–d) show velocity histograms for stars in three  $[\text{Fe}/\text{H}]$  bins: (b)  $[\text{Fe}/\text{H}] \geq -0.5$ , (c)  $-1.0 < [\text{Fe}/\text{H}] < -0.5$ , and (d)  $[\text{Fe}/\text{H}] \leq -1.0$ . The strength of the cold component in each metallicity bin is measured by performing a maximum-likelihood

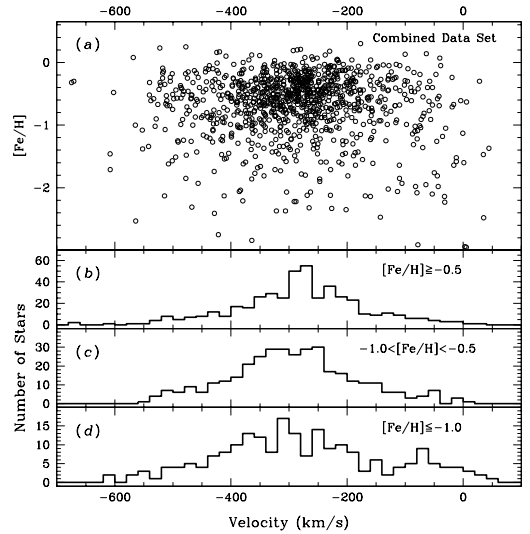


FIG. 10.— (a) Metallicity vs. heliocentric velocity for the full M31 RGB sample. The majority of the population is metal-rich, with an evenly distributed metal-poor tail over the full range of velocities. A concentration of metal-rich stars near  $v_{\text{hel}} = -300 \text{ km s}^{-1}$  can be seen. The bottom three panels show velocity histograms for subsets of the data: (b)  $[\text{Fe}/\text{H}] \geq -0.5$ , (c)  $-1.0 < [\text{Fe}/\text{H}] < -0.5$ , and (d)  $[\text{Fe}/\text{H}] \leq -1.0$ . The  $\sim -300 \text{ km s}^{-1}$  cold component is more dominant in the metal-rich samples. A maximum-likelihood double-Gaussian fit was performed for each subset of the data, with all of the parameters except  $N_{\text{sub}}/N_{\text{tot}}$  held fixed at the best-fit values for the complete M31 RGB sample (§ 4.1, Fig. 4, Table 2). The cold component comprises a negligible fraction of the population in (d), 20.9% of the population in (c), and 29.2% of the population in (b), indicating that the  $\sim -300 \text{ km s}^{-1}$  cold component is relatively metal-rich.

double-Gaussian fit to the velocity distribution. Only the fraction of stars in the cold component ( $N_{\text{sub}}/N_{\text{tot}}$ ) is allowed to vary; the rest of the parameters are held fixed at the best-fit values from the fit to the full M31 RGB sample (§ 4.1, Table 2). The fraction of stars in the cold component is 29.2% in (b), 20.9% in (c), and is negligible in (d), indicating that the cold component is metal-rich relative to the dynamically hot component.

Figure 11 compares the metallicity distributions of stars in the velocity range of the  $\sim -300 \text{ km s}^{-1}$  cold component (*solid line*) discovered in fields H11, f116, and f123 and stars that are identified with the hot spheroidal component (*dashed line*) in those fields. The hot spheroidal distribution ( $v_{\text{outer}}$ ) is based on stars whose velocities are greater than  $\pm 2\sigma_v^{\text{sub}}$  away from  $\langle v \rangle^{\text{sub}}$ . This minimizes contamination of the spheroidal component by stars associated with the  $\sim -300 \text{ km s}^{-1}$  cold component. An additional constraint on the  $v_{\text{outer}}$  distribution is that only stars with  $v_{\text{hel}} < -150 \text{ km s}^{-1}$  are included in order to avoid residual MW dwarf star contaminants that lie in the range  $v_{\text{hel}} > -150 \text{ km s}^{-1}$  (§ A.2). Stars within the velocity range of the cold component can only statistically be identified as belonging to the hot spheroid or cold component, thus it is not possible to identify an uncontaminated sample of the  $\sim -300 \text{ km s}^{-1}$  cold component. Stars with velocities within  $\pm 1\sigma_v^{\text{sub}}$  of  $\langle v \rangle^{\text{sub}}$  are used for the  $v_{\text{inner}}$   $[\text{Fe}/\text{H}]$  distribution, in order to maximize the number of members of the cold component while minimizing the contribution of spheroid stars.

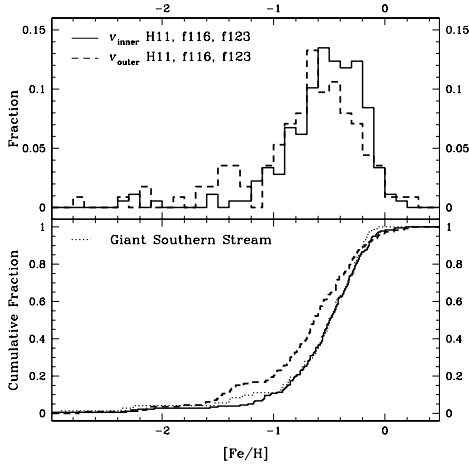


FIG. 11.— The  $[\text{Fe}/\text{H}]$  distribution of the  $v_{\text{inner}}$  (solid line) and  $v_{\text{outer}}$  (dashed line) components in fields H11, f116, and f123, in histogram (top) and cumulative (bottom) form. The  $v_{\text{inner}}$  (cold component) sample is defined to be stars with velocities within the range  $\langle v \rangle^{\text{sub}} - \sigma_v^{\text{sub}} < v_{\text{hel}} < \langle v \rangle^{\text{sub}} + \sigma_v^{\text{sub}}$ , where  $\langle v \rangle^{\text{sub}}$  and  $\sigma_v^{\text{sub}}$  represent the best-fit narrow Gaussian components in each field. This range was chosen to maximize the percentage of substructure stars compared to hot spheroid stars. The  $v_{\text{outer}}$  (hot spheroid) sample consists of stars with velocities  $v_{\text{hel}} < \langle v \rangle^{\text{sub}} - 2\sigma_v^{\text{sub}}$  or  $\langle v \rangle^{\text{sub}} + 2\sigma_v^{\text{sub}} < v_{\text{hel}} < -150 \text{ km s}^{-1}$ . This minimizes contamination from substructure stars and spheroid populations (§ A.2) in the hot spheroidal  $[\text{Fe}/\text{H}]$  distribution. The  $v_{\text{inner}}$  sample is slightly more metal rich than the  $v_{\text{outer}}$  sample. Since the  $v_{\text{inner}}$  sample is contaminated by spheroid stars, the true difference in  $[\text{Fe}/\text{H}]$  between the substructure and spheroid populations is somewhat greater than indicated in this plot. The cumulative  $[\text{Fe}/\text{H}]$  distribution of stars in M31’s GSS (from fields at 33 and 21 kpc; Guhathakurta et al. 2006; Kalirai et al. 2006a) is plotted in the bottom panel for comparison (thin dotted line), and will be discussed in § 7.1.

The  $[\text{Fe}/\text{H}]$  distribution of the  $v_{\text{outer}}$  sample has a peak at lower  $[\text{Fe}/\text{H}]$  values and a larger metal-poor tail than the  $[\text{Fe}/\text{H}]$  distribution of the  $v_{\text{inner}}$  sample. The mean (median) metallicity of the  $v_{\text{outer}}$  sample is  $\langle [\text{Fe}/\text{H}] \rangle_{\text{mean}} = -0.72$  ( $\langle [\text{Fe}/\text{H}] \rangle_{\text{med}} = -0.63$ ), while the mean (median) metallicity of the  $v_{\text{inner}}$  sample is  $\langle [\text{Fe}/\text{H}] \rangle_{\text{mean}} = -0.55$  ( $\langle [\text{Fe}/\text{H}] \rangle_{\text{med}} = -0.49$ ). A KS test returns a probability of 0.7% that the two distributions are drawn from the same parent distribution. The  $v_{\text{inner}}$  distribution is highly contaminated by spheroid stars even within  $\pm 1\sigma_v^{\text{sub}}$  of  $\langle v \rangle^{\text{sub}}$  (Fig. 6); the estimated contamination of the  $v_{\text{inner}}$  sample by spheroid stars is 32.5%. A statistical subtraction of the  $v_{\text{outer}}$  distribution (scaled by the contamination rate) from the  $v_{\text{inner}}$  distribution yields a distribution with a mean (median) metallicity of  $\langle [\text{Fe}/\text{H}] \rangle_{\text{mean}} = -0.52$  ( $\langle [\text{Fe}/\text{H}] \rangle_{\text{med}} = -0.45$ ).

An important effect on the measured  $[\text{Fe}/\text{H}]$  values is the assumed age (12 Gyr) of the stellar population. This assumption is wrong for at least field H11, which has been shown by deep HST/ACS imaging to contain a wide spread of stellar ages, ranging from 6–13.5 Gyr (Brown et al. 2003, 2006b). Our data show a sharp cutoff in the  $[\text{Fe}/\text{H}]$  distribution at  $[\text{Fe}/\text{H}] \sim 0$ , with a metal-poor tail that extends out to  $[\text{Fe}/\text{H}] \sim -1.5$  to  $-2.0$  (Fig. 11). The Brown et al. (2006b) HST/ACS data show a metal-rich cutoff in the  $[\text{Fe}/\text{H}]$  distribution at  $[\text{Fe}/\text{H}] \sim 0.3$ , with a metal-poor tail which extends to  $[\text{Fe}/\text{H}] \sim -1.5$  to  $-2.0$  (Fig. 9 of Brown et al. (2006b)). The star formation

history derived from the HST/ACS CMDs show that the intermediate age population (6–9 Gyr) is metal-rich ( $[\text{Fe}/\text{H}] \sim 0$ ), while the old (10–14 Gyr) stellar population is relatively metal-poor. Thus, our assumed age of 12 Gyr will underestimate metallicities for stars with  $[\text{Fe}/\text{H}]$  values near solar, but is appropriate for the more metal-poor stars ( $[\text{Fe}/\text{H}] \lesssim -0.5$ ). Varying the age between 6 and 14 Gyr introduces an  $\approx 0.3$ – $0.4$  dex spread in the  $[\text{Fe}/\text{H}]$  values derived from the isochrone fitting (Kalirai et al. 2006b); after accounting for this offset at the metal-rich end of the  $[\text{Fe}/\text{H}]$  distribution, our  $[\text{Fe}/\text{H}]$  distribution is consistent with the Brown et al. (2006b) result.

The intrinsic spread in ages in the spheroid found by Brown et al. (2003, 2006b) can have two possible effects on our comparison of the  $[\text{Fe}/\text{H}]$  distributions of the  $v_{\text{inner}}$  and  $v_{\text{outer}}$  samples. If all the stars in these fields have a common spread in ages regardless of their kinematical properties, the error in the  $[\text{Fe}/\text{H}]$  measurement introduced by assuming a uniform age for the population will cause a shift in the actual  $[\text{Fe}/\text{H}]$  values, but the relative difference between the  $v_{\text{inner}}$  and  $v_{\text{outer}}$  populations will not be greatly affected. If the stars associated with the  $\sim -300 \text{ km s}^{-1}$  cold component are systematically younger than the underlying smooth spheroid population, the measurement of  $[\text{Fe}/\text{H}]$  for the  $v_{\text{inner}}$  sample derived from the 12 Gyr isochrones will be biased towards low metallicities, and thus the intrinsic difference in metallicity between the two populations will be greater than shown.

We have also assumed that all stars are at the same line-of-sight distance as M31’s center. This is a valid approximation for the inner spheroid: at  $R_{\text{proj}} = 20 \text{ kpc}$ , the spread in line-of-sight distances is expected to be about  $\pm 20 \text{ kpc}$  (a spread in apparent magnitude of  $\pm 0.05 \text{ dex}$ ), which corresponds to a spread in  $[\text{Fe}/\text{H}]$  of approximately  $\pm 0.03 \text{ dex}$ . If the cold component is systematically more (less) distant than M31’s spheroid (§ 7.1), the intrinsic difference in metallicity between the populations will be slightly smaller (greater).

Although fields f115 and f135 do not show clear evidence of substructure (§ 4.2), they are both within the minor axis range of the  $\sim -300 \text{ km s}^{-1}$  cold component (Fig. 9; § 6.1). If the cold components in fields H11, f116, and f123 have the same physical origin, it is reasonable to postulate that there may be substructure in fields f115 and f135 that is not detected by the fits to the radial velocity distributions. The stars in fields f115 and f135 that fall within the triangular region marked in the upper panel of Figure 9 have mean (median)  $[\text{Fe}/\text{H}]$  values of  $-0.67$  ( $-0.57$ ) and  $-0.56$  ( $-0.46$ ), respectively. Stars from fields f115 and f135 that have velocities both outside the triangular region and  $v_{\text{hel}} < -150 \text{ km s}^{-1}$  have mean (median)  $[\text{Fe}/\text{H}]$  values of  $-0.61$  ( $-0.53$ ) and  $-0.64$  ( $-0.59$ ), respectively. The  $[\text{Fe}/\text{H}]$  distributions of stars in fields f135 and f115 that are within the triangular region of the  $\sim -300 \text{ km s}^{-1}$  cold component are consistent with both the  $v_{\text{inner}}$  and  $v_{\text{outer}}$  distributions. The difference between the substructure and spheroid metallicity distributions is small, and is only statistically significant when the three fields contributing to the  $\sim -300 \text{ km s}^{-1}$  cold component are combined (into the  $v_{\text{inner}}$  and  $v_{\text{outer}}$  samples). The number of stars within a restricted ve-

locity range in any given field is too small to support a statistically significant comparison.

### 6.3. Comparison to Previous Observations

The H11 field has been presented in previous papers as a smooth spheroid field that is well-described by a single, kinematically hot component (Brown et al. 2006a,b; Kalirai et al. 2006a). There are two related factors that have caused this field to be reinterpreted as containing substructure. First, the data set presented in this paper represents an order of magnitude increase in the sample size of confirmed M31 RGB stars over previous spectroscopic samples published by our group in the SE minor axis region of the inner spheroid ( $R_{\text{proj}} \lesssim 30$ ). Only the H11 and a0 fields have been previously published, and the data published in H11 contained only a fraction of the full data set for that field, based on preliminary reductions (§ 2.2.2). This paper presents the full H11 data set and combines it with new data from neighboring fields. Second, the triangular shape of the  $\sim -300 \text{ km s}^{-1}$  cold component in a plot of velocity vs. position along the minor axis implies that the debris has a relatively large velocity dispersion in the H11 field. This makes the debris harder to detect against the broad underlying spheroid than if it were kinematically colder. The increase in the sample size of stars with recovered velocities in the H11 field, coupled with the context provided by the velocity distributions in neighboring fields, has proved to be crucial in detecting the substructure in H11.

Previous observational studies have suggested the possibility of substructure along M31’s southeastern minor axis. Reitzel & Guhathakurta (2002) found a dynamically cold grouping of 4 metal-rich M31 RGB stars (out of  $\sim 35$ ) along a southeastern minor axis field at  $R_{\text{proj}} \sim 19 \text{ kpc}$ . This hint of substructure was strengthened by subsequent observations at 7 and 11 kpc along the southeastern minor axis, which increased the total M31 RGB sample to  $\sim 100$  stars (Guhathakurta 2002). The star-count maps in Ferguson et al. (2002) (their Fig. 2) also show hints of a population of metal-rich stars along the southeastern minor axis, and deep HST/ACS imaging has discovered a significant intermediate-age population in field H11 (§ 8, Brown et al. 2003). With the spectroscopic sample of  $> 1000$  stars presented in this paper, we are able to confidently identify a cold component along the southeastern minor axis and characterize its properties.

## 7. PHYSICAL ORIGIN OF THE COLD COMPONENT

The observed M31 RGB population along the southeastern minor axis exhibits a spatially varying kinematically cold component, which has a higher mean metallicity than the underlying inner spheroid population. A cold component with these properties could be part of the outskirts of M31’s disrupted disk or debris left by disrupted satellites. The models of F07 predict debris stripped from the progenitor of the GSS should be present in these fields. (It is also possible, of course, that the observed substructure is satellite debris *unrelated* to the GSS.) This section examines both the continuation of the GSS (§ 7.1) and M31’s disturbed disk (§ 7.2) as possible physical origins of the cold component.

### 7.1. Relation to the Giant Southern Stream

#### 7.1.1. Model of a Recent Interaction

Debris in the form of coherent shells has been observed in many elliptical galaxies; these shells are believed to be formed by the tidal disruption of a satellite galaxy on a nearly radial orbit (e.g., Schweizer 1980; Hernquist & Quinn 1988; Barnes & Hernquist 1992). F07 presents the hypothesis that the Northeast and Western “shelves” observed in M31 (Fig. 1, also see Fig. 1 of F07) are a similar phenomenon to these shell systems, and have been created by the disruption of the progenitor of the GSS. Shells have coherent velocities, and display a distinctive triangular shape in the  $v_{\text{los}}$  vs.  $R_{\text{proj}}$  plane (Merrifield & Kuijken 1998, F07). In general, as  $R_{\text{proj}}$  approaches the boundary of the shell the spread in velocities approaches zero, with the mean velocity at the tip of the triangle expected to be at the systemic velocity of the system.

F07 present an  $N$ -body simulation of an accreting dwarf satellite within M31’s potential. The simulations use a static bulge+disk+halo model which is based on the M31 mass models in Geehan et al. (2006) combined with the observed stellar density distribution in the halo (Guhathakurta et al. 2005), and assumes an isotropic velocity distribution in the outer halo. The simulated satellite’s physical and orbital properties have been chosen to reproduce the observed properties of the GSS and Northeast shelf, using the methods of Fardal et al. (2006). The simulations show that the orbit which reproduces these features also reproduces a photometric feature identified in F07 as the “Western shelf” and an observed stream of counter-rotating planetary nebulae (Merrett et al. 2003, 2006).

Figure 12 shows the projected sky positions (in M31-centric coordinates) of the satellite particles from the F07 simulation. The particles are color-coded by shell, or equivalently, by the number of pericentric passages they have made. Green particles represent particles approaching their first pericentric passage; they correspond to the observed GSS. Red particles correspond to the observed Northeast shelf; they are between their first and second pericentric passages. Magenta particles represent the Western shelf identified in F07, and are between their second and third pericentric passages. The blue particles are between their third and fourth pericentric passages, and represent the “Southeast shelf” predicted by F07. This last feature is predicted to extend out to a radius of 18 kpc and is expected to be very faint, as it consists of particles further forward in the continuation of the stream than the more visible Northeast and Western shelves. This feature actually covers  $\sim 180^\circ$  in position angle on the east side of M31, although it is likely to only be visible in the southeast due to its overlap with the Northeast shelf and M31’s disk. In the F07 simulations, the Northeast shelf is made up of both the leading material from the progenitor’s first pericentric passage and trailing material from its second pericentric passage, while the Western shelf is formed by leading material. The simulations are unable to constrain whether or not the satellite disrupts completely, as this is dependent on the central density of the satellite.

The bottom panel of Figure 13 presents the distribution of particles from the F07 simulation in the  $v_{\text{los}}$  vs.  $R_{\text{proj}}$  plane. The figure shows particles related to the

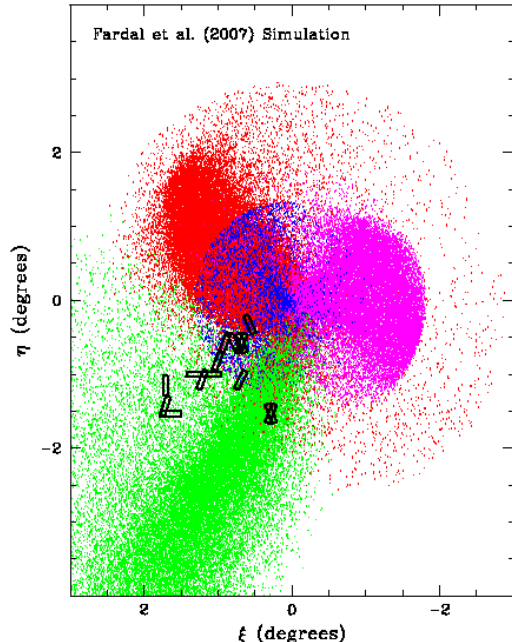


FIG. 12.— Projected sky position (in M31 centric coordinates  $\xi$  and  $\eta$ ) of tidal debris in the F07 simulations of the merger of a dwarf galaxy with M31. Particles approaching their first pericentric passage are part of the GSS (green). Particles approaching their second pericentric passage form the Northeast shelf (red), and particles approaching their third pericentric passage form the Western shelf (magenta) identified in F07. Particles in blue are approaching their fourth pericentric passage, and form a faint shelf feature which is predicted to be most easily visible in the southeast. The position of our spectroscopic masks are also shown; fields f123 and f135 straddle the edge of the Southeast shelf (Fig. 2). The two masks at  $\xi = 0.3^\circ$ ,  $\eta = -1.5^\circ$  are in field H13s, which is discussed in § 7.1.3 and § 8.

merging satellite as well as particles associated with the static bulge+disk+stellar-halo M31 model used in F07. In order to carry out a precise comparison to our observational data set, the F07 simulation particles were selected based on their projected sky position; all particles that fall inside a  $16' \times 10'$  area (the approximate area of one DEIMOS mask is  $16' \times 4'$ ) centered on the position of our observed fields, and oriented at the position angle of our observed masks, are displayed. The satellite particles are color-coded by shell (or, equivalently, the number of orbits they have made) as in Figure 12. Green particles are associated with the GSS, red particles with the Northeast shelf, and black particles with the bulge+disk+stellar-halo model for M31. The blue particles, which are part of the predicted “Southeast” shelf, form the distinctive triangular shape expected of a shell feature in the  $R_{\text{proj}}-v_{\text{los}}$  plane.

In the following discussion, it is important to distinguish between “spillover” from the GSS (material associated with the GSS that is in roughly the same orbital phase as the material in the GSS, i.e., green particles in Figs. 12 & 13) versus wrapped around portions of the GSS (material associated with the GSS progenitor that is leading the GSS and has undergone one or more additional pericentric passages, i.e., red, magenta and blue particles in Figs. 12 & 13). The latter is the main theme of this paper, although we also briefly discuss the former

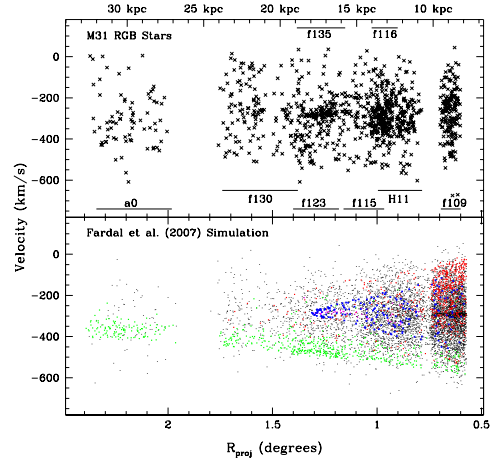


FIG. 13.— Line-of-sight velocity vs. projected radial distance from M31’s center ( $R_{\text{proj}}$ ) of spectroscopically confirmed M31 RGB stars (*top panel*) and particles from the F07 simulations of the orbit of the progenitor of the GSS (*bottom panel*). Particles are drawn from the locations of each of our DEIMOS masks. The area from which particles have been drawn has been increased relative to the size of a slitmask to increase the number of particles. The satellite particles are color-coded according to which shell they are in: the giant southern stream (green), the Northeast shelf (red), and the predicted Southeast shelf (blue). Black points are particles from the bulge+disk+stellar-halo of M31. The blue particles form a triangular shape, with an increasingly wide kinematic profile as the minor axis distance to the center of M31 decreases, as seen in the data. The tip of the triangle at  $R_{\text{proj}} \sim 1.3^\circ$  (18 kpc) in the simulated data agrees well with the observed tip in the data in field f123. The cold concentration of M31 particles at  $v_{\text{M31}} \approx 0 \text{ km s}^{-1}$  extending from  $R_{\text{proj}} \sim 0.58^\circ$  to  $\sim 0.73^\circ$  (7.9 to 10.0 kpc) corresponds to the disk of M31 (*bottom panel*); the kinematical signature of a smooth, cold disk is not seen in our data (*top panel*).

in §§ 7.1.2–7.1.3.

### 7.1.2. Comparison of Model to Data

#### SKY POSITION

Figure 12 shows the projected sky positions (in M31-centric coordinates) of the satellite particles from the F07 simulation as well as the size, position and orientation of our Keck/DEIMOS slitmasks (*rectangles*). Fields f123 and f135 land on the edge of the predicted Southeast shelf (*blue particles*), fields f115, f116, H11 and f109 all lie within the boundary of the Southeast shelf, and fields f130 and a0 lie beyond it. Thus, the model predicts that the edge of the shell feature should pass directly through our CFHT/MegaCam image. Indeed, there is an apparent edge visible in the CFHT starcount map (Fig. 2, passing through field f123), in the same location as that predicted for the Southeast shelf. A close inspection of the Ibata et al. (2005) starcount map (Fig. 1) reveals a point of bifurcation between the edge of the Northeast shelf and a fainter feature at  $\xi \approx 1.6^\circ$ ,  $\eta \approx 0.2^\circ$ , in rough agreement with the bifurcation of the two features in Figure 12. This bifurcation is more evident in the Sobel-filtered map in F07 (their Fig. 1). The radii of the shells in the simulation are robust (§ 4.2 of F07); thus the agreement between the observations and the simulations is a strong confirmation of the validity of the F07 model.

#### KINEMATIC TRENDS

The  $\sim -300 \text{ km s}^{-1}$  cold component observed in our minor axis fields shows the distinctive triangular velocity pattern expected of a shell feature in the  $R_{\text{proj}}-v_{\text{los}}$  plane. Figure 13 compares our data (top panel) to the F07 model (bottom panel). The distribution of observed velocities narrows to a tip at  $R_{\text{proj}} \approx -1.3^\circ$  (18 kpc) in the simulated particle distribution, which is similar to the position of the tip of the velocity distribution in our observed data. At  $R_{\text{proj}} \approx -1^\circ$  (13.7 kpc), the velocity distribution of the observed substructure has widened to a spread of  $\sim 200 \text{ km s}^{-1}$  (measured from the edges of the feature), also in agreement with the velocity spread of the predicted Southeast shelf.

The “boxy” shape of the velocity distribution in field H11 (Fig. 6) is also consistent with the interpretation of the substructure as being part of a shell system. The velocity distributions of shells have a clearly defined minimum and maximum line-of-sight velocity at a given  $R_{\text{proj}}$ . Stars tend to congregate at the minimum and maximum velocities (Merrifield & Kuijken 1998, F07), although their location in the  $R_{\text{proj}}-v_{\text{los}}$  plane depends on the region they occupy in space (cf. the discussion in F07).

A maximum-likelihood Gaussian fit to the particles identified with the Southeast shelf and within the minor axis distance spanned by field f123 yields parameters of  $\langle v \rangle = -280.6 \text{ km s}^{-1}$  and  $\sigma_v = 19.4 \text{ km s}^{-1}$ . A Gaussian fit to the Southeast shelf particles within the minor axis range spanned by fields f116 and H11 returns  $\langle v \rangle = -292.6 \text{ km s}^{-1}$  and  $\sigma_v = 60.5 \text{ km s}^{-1}$ . The mean velocity and dispersion of the predicted shelf is in good agreement with the properties of the observed substructure (Table 2).

#### METALLICITY DISTRIBUTION

If the substructure identified in this paper is part of the predicted Southeast shelf in F07, it should have a similar metallicity distribution to that of the GSS, since the two structures originated from the same progenitor. As part of our Keck/DEIMOS survey of M31’s inner spheroid and halo, we have taken spectra in two fields located on the GSS: a field at  $R_{\text{proj}} = 33 \text{ kpc}$  (Guhathakurta et al. 2006) and a field at  $R_{\text{proj}} = 21 \text{ kpc}$  (H13s; Kalirai et al. 2006a). The cumulative  $[\text{Fe}/\text{H}]$  distribution of stars identified kinematically as belonging to the GSS in these two fields is plotted in the bottom panel of Figure 11 (thin dotted line). It is very similar to the  $[\text{Fe}/\text{H}]$  distribution of stars that are kinematically associated with the substructure in fields H11, f116, and f123. The mean and median  $[\text{Fe}/\text{H}]$  of the stars in the GSS are 0.1 and 0.05 dex more metal-poor, respectively, than the mean and median  $[\text{Fe}/\text{H}]$  of the substructure in fields H11, f116, and f123, after correcting for spheroid contamination (§ 6.2). The estimated number of inner spheroid star contaminants in the GSS sample is a few stars (Guhathakurta et al. 2006; Kalirai et al. 2006a). If the 3 most metal-poor stars are removed ( $[\text{Fe}/\text{H}] < -2.25$ ) from the GSS distribution, the mean and median metallicity of the GSS stars are only 0.01 dex more metal-poor than the the minor axis substructure. The  $[\text{Fe}/\text{H}]$  values of the GSS stars have not been corrected for the GSS’ measured distance relative to M31 ( $\sim 50 \text{ kpc}$  behind M31 for these 2 fields; McConnachie et al. 2003). Accounting for this effect would decrease the average metallicity of the GSS by

$\sim 0.1$  dex. The distance to the minor axis substructure is not known, although the F07 simulations predict that the Southeast shelf should be approximately at M31’s distance, with a spread in distances of  $\pm 9.2 \text{ kpc}$  (this corresponds to  $\pm 2\sigma$  in terms of the distribution of particle distances).

#### STRENGTH OF THE COLD COMPONENT

The cold component comprises 44% of the total population of observed stars in fields H11 and f116 and 31% of observed M31 RGB stars in field f123 (Table 2). This corresponds to a lower limit for the total fraction of stars in the cold component of 21.7% in the fields within the predicted range of the Southeast shelf (f109, H11, f116, f115, f123, and f135). The Southeast shelf in the simulations is much weaker, comprising only 2.7% of the total population in these fields (this number increases to 3.4% if the number of shelf particles is compared only to the number of bulge+disk+stellar-halo M31 particles). The strength of the feature in the simulations is highly dependent on the mass of the progenitor and the time since the first collision (F07). Thus, the strength of the observed substructure will place interesting constraints on future models of the stream, but cannot be used as a reliable discriminant of the applicability of the model at the present time.

#### FIELDS WITHOUT CLEAR DETECTION OF SUBSTRUCTURE

We do not find a clear detection of substructure in fields f130 and a0. In the context of the Southeast shelf, this is not surprising as both these fields are beyond the radial range spanned by the shelf (Fig. 12). Field f109 is significantly inward of the innermost field in which we detect substructure. In the simulation, the particles associated with the Southeast shelf continue into the region covered by field f109 with a spread in velocities of  $\sim 350 \text{ km s}^{-1}$  (Fig. 13, bottom panel). The data in field f109 is consistent with being drawn from a single Gaussian (§ 4.2) and shows no evidence of substructure. A secondary component with a spread in velocities as wide as predicted would be very difficult to differentiate from the broad spheroidal component, and would require a much larger sample of M31 RGB stars in this field than is currently available.

Field f115 is well within the boundaries of the Southeast shelf. As discussed in § 6.1, its velocity distribution is consistent with being drawn from the same parent distribution as field f116. The shell in field f115 may be difficult to detect in our data due to the broad ( $\sim 55 \text{ km s}^{-1}$ ) nature of the substructure and the smaller number of stars available in this field ( $\sim 50\%$  less than in field f116), or the shelf may be inherently clumpy.

Field f135 is on the edge of the simulated shelf, and shows evidence for a peak of stars near  $v_{\text{hel}} \sim -300 \text{ km s}^{-1}$  in its radial velocity histogram. In light of the simulations, we discuss this field in detail in § 7.1.3, and show that it may contain a kinematically-cold component whose properties are consistent with both the observations of the  $\sim -300 \text{ km s}^{-1}$  cold component in fields H11, f116, and f123 and the simulations of the Southeast shelf.

#### DEBRIS FROM THE GSS

The GSS is observed to have an asymmetric shape, with a sharp edge on the eastern side and a more gradual decline in density on the western side (McConnachie et al. 2003). However, the eastern edge is not an absolute one in the models, and “spillover” material from the GSS (§ 7.1) is predicted by the F07 simulations to be present in all of our fields. Field f135 is the closest of our fields to the GSS’ eastern edge (Figs. 1 and 12); § 7.1.3 discusses the evidence for spillover debris from the GSS in this field.

Since the density of M31 RGB spheroid stars falls off strongly with increasing radius in the inner spheroid, the contrast of cold GSS debris against the dynamically hot spheroid is expected to be greatest in our outermost field, a0. The GSS debris in field a0 is predicted to have a mean velocity of  $\langle v \rangle_{\text{GSS}} = -364 \text{ km s}^{-1}$ . Although field a0 shows hints of peaks in the radial velocity distribution at  $v_{\text{hel}} < -300 \text{ km s}^{-1}$  (Fig. 6), only a handful of these stars are as metal-rich as the GSS ( $[\text{Fe}/\text{H}] \gtrsim -0.75$ ). This allows us to place an upper limit on the contamination of field a0 by the GSS of  $\lesssim 5$  stars ( $\lesssim 6\%$ ).

Although the F07 simulations reproduce many of the observations in the GSS, they predict a much larger amount of debris on the eastern side than is observed in our fields (Fig. 13). Many factors can influence the structure of the debris in the simulations, including the shape and rotation of the progenitor. The current models of the stream (F07) use a spherical, non-rotating progenitor. A more complex model of the progenitor may be required to reproduce the observations (Fardal et al., private communication).

### 7.1.3. Evidence of the Southeast Shelf and Spillover Debris from the GSS in Field f135

The F07 simulations predict that in addition to the Southeast shelf some spillover debris associated with the GSS (§ 7.1) should be present in field f135. The sky coordinates of field f135 are  $\xi = 0.7$ ,  $\eta = -1.1$ , which places it on the edge of both the GSS and the Southeast shelf in the F07 simulations (Figure 12). In addition, the radial velocity distribution of stars in field f135 is not well-fit by either a single or double Gaussian (§ 4.2) and shows evidence of a metal-rich population (§ 6.2). Motivated by the close match between the observations and simulations of substructure in fields H11, f116 and f123, we carry out a constrained fit of the radial velocity histogram of field f135 to the sum of three Gaussians to determine if the Southeast shelf is present in this field.

The mean velocity and velocity dispersion of the simulated Southeast shelf and GSS particles in field f135 are  $\langle v \rangle_{\text{SE}} = -286 \text{ km s}^{-1}$ ,  $\sigma_v^{\text{SE}} = 19 \text{ km s}^{-1}$  and  $\langle v \rangle_{\text{GSS}} = -458 \text{ km s}^{-1}$ ,  $\sigma_v^{\text{GSS}} = 40 \text{ km s}^{-1}$ . These values were used as rough constraints for the triple Gaussian fit: the means were allowed to vary within  $\pm 100 \text{ km s}^{-1}$  of the predicted values and the dispersions were allowed to vary from  $1 \text{ km s}^{-1}$  to  $3\sigma_v^{\text{SE}}$  and  $2\sigma_v^{\text{GSS}}$ . The wide Gaussian component parameters were held fixed at the values for  $G^{\text{sph}}(v)$ :  $\langle v \rangle^{\text{sph}} = -287.2 \text{ km s}^{-1}$  and  $\sigma_v^{\text{sph}} = 128.9 \text{ km s}^{-1}$  (§ 4.1). The maximum-likelihood triple Gaussian fit is displayed in Figure 14 (*solid curve*). The wide underlying inner spheroid component ( $G^{\text{sph}}(v)$ , *dot-dashed curve*) comprises 45% of the population. The Southeast shelf component (*dashed curve*), which is the

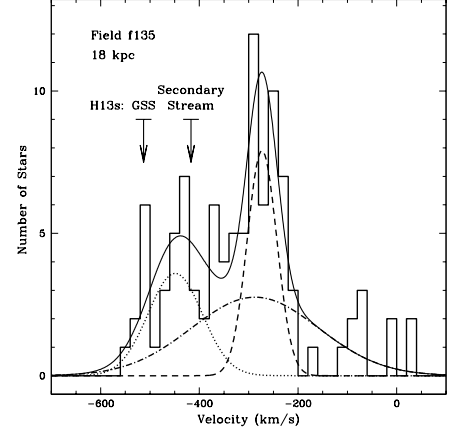


FIG. 14.— Radial velocity histogram of M31 RGB stars in field f135. A constrained triple Gaussian (*solid curve*) has been fit to the observed data using a maximum-likelihood technique, with rough constraints imposed on the parameters based on the properties of the simulated substructure (§ 7.1.3). The observed velocity distribution is well fit by a sum of three Gaussians: (i)  $G^{\text{sph}}(v)$ , the wide Gaussian which corresponds to the underlying inner spheroid of M31 (*dot-dashed curve*, § 4.1), (ii) a component centered at  $\langle v \rangle^{\text{sub}} = -273 \text{ km s}^{-1}$  with a width of  $\sigma_v^{\text{sub}} = 30 \text{ km s}^{-1}$ , which comprises 30% of the total population and which likely corresponds to the Southeast shelf (*dashed curve*), and (iii) a narrow component centered at  $\langle v \rangle = -449 \text{ km s}^{-1}$  with a width of  $\sigma_v = 55 \text{ km s}^{-1}$ , which comprises 25% of the total population (*dotted curve*). The mean velocity and velocity dispersion ( $\pm 1\sigma_v$ ) of the cold components in field H13s, at a similar radial distance along the GSS as field f135, are shown as arrows and horizontal lines (§ 7.1.3; Kalirai et al. 2006a).

narrow peak at  $\langle v \rangle^{\text{sub}} = -273 \text{ km s}^{-1}$ , comprises 30% of the population and has a width of  $\sigma_v^{\text{sub}} = 30 \text{ km s}^{-1}$ . The “GSS” component (*dotted curve*) at  $\langle v \rangle = -449 \text{ km s}^{-1}$  has a dispersion of  $\sigma_v = 55 \text{ km s}^{-1}$  and comprises 25% of the total population. If a more constrained fit is carried out with the  $\langle v \rangle$  and  $\sigma_v$  parameters for all three Gaussian components held fixed (at the predicted values for the simulated shelf and stream particles and at the parameters of the Gaussian  $G^{\text{sph}}(v)$ ) and only the fractions of stars in the various components are allowed to vary, the best-fit distribution has  $N_{\text{shelf}}/N_{\text{tot}} = 0.18$  and  $N_{\text{GSS}}/N_{\text{tot}} = 0.17$ .

The kinematic properties (mean velocity and velocity dispersion) of the Southeast shelf component in the triple Gaussian fit to field f135 are consistent not only with the simulations, but also with what one would expect for the Southeast shelf in this field based on the observations (e.g., Fig. 13, Table 2). In addition, the fraction of the population in f135 which is in this component is consistent with the fraction of the population which is identified with the Southeast shelf in fields H11, f116, and f123. As further evidence that the Southeast shelf is detected in field f135, Figure 15 shows  $[\text{Fe}/\text{H}]$  vs.  $v_{\text{hel}}$  for the M31 RGB stars in field f135 (panel a), as well as velocity histograms for stars in two  $[\text{Fe}/\text{H}]$  bins [(b)  $[\text{Fe}/\text{H}] > -0.75$  and (c)  $[\text{Fe}/\text{H}] < -0.75$ ]. As in fields H11, f116 and f123, the substructure in field f135 that is identified with the Southeast shelf ( $\langle v \rangle = -273 \text{ km s}^{-1}$ ) is relatively metal-rich.

The velocity dispersion of  $\sigma_v = 55 \text{ km s}^{-1}$  for the “GSS component” inferred from the first of the triple-Gaussian



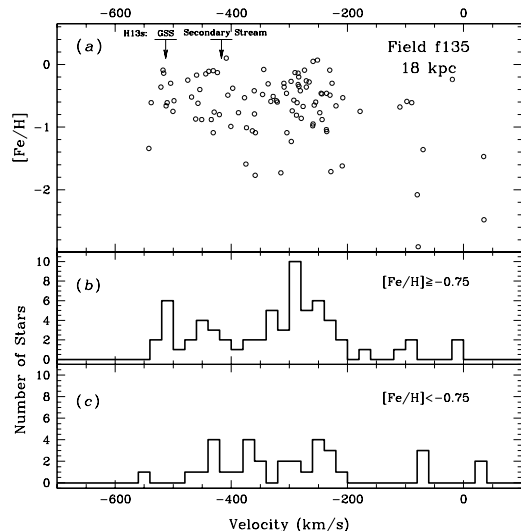


FIG. 15.— (a) Metallicity vs. heliocentric velocity for the M31 RGB stars in field f135, which lies to the east of the edge of the GSS. The mean velocities and dispersions ( $\pm 1\sigma_v$ ) of the GSS and the secondary stream from the GSS field H13s (Kalirai et al. 2006a) are marked, as in Figure 14. (b) Velocity distribution of stars with  $[Fe/H] \geq -0.75$ . In addition to the  $\sim -300$  km s $^{-1}$  cold component, the metal-rich subset shows evidence of concentrations of stars corresponding to the GSS and secondary stream in the H13s field. (c) Velocity distribution of stars with  $[Fe/H] < -0.75$ . The velocities of stars with metallicities lower than  $-0.75$  dex appear evenly distributed.

fits above is large compared to previous measurements of  $\sim 15$  km s $^{-1}$  for the dispersion of the GSS (Ibata et al. 2004; Guhathakurta et al. 2006; Kalirai et al. 2006a). In addition, although the best-fit  $\langle v \rangle^{\text{sub}}$  of the most negative component in f135 is similar to that of the F07 model, the predicted GSS mean velocities in the F07 model are not as negative as the observed velocities of the GSS. Kalirai et al. (2006a) analyzed a field centered on a high surface brightness portion of the GSS, at approximately the same radial distance along the stream as field f135 (field H13s, located at  $\xi = 0.3^\circ$ ,  $\eta = -1.5^\circ$  in Figure 12) and found a secondary cold component, the “H13s secondary stream,” whose origin and physical extent are unknown. The observed mean velocities of the GSS and secondary stream in the H13s field are  $\langle v \rangle^{\text{GSS}} = -513$  km s $^{-1}$  and  $\langle v \rangle^{\text{sec.str.}} = -417$  km s $^{-1}$ , respectively, with velocity dispersions of  $\sigma_v^{\text{GSS}} = \sigma_v^{\text{sec.str.}} = 16$  km s $^{-1}$  (Kalirai et al. 2006a). The mean velocities and velocity dispersions ( $\pm 1\sigma_v$ ) of these two components are shown as arrows with horizontal lines in Figures 14 and 15. There appear to be two metal-rich peaks in f135 with the approximate velocities of the GSS and secondary stream in H13s. If both the GSS and H13s secondary stream are present in field f135, they appear in approximately equal proportion. In H13s the GSS dominates over the secondary stream by a factor of two (Kalirai et al. 2006a).

In the simulations, the GSS dominates over the Southeast shelf in field f135 by about a factor of 10; the observations indicate that, at best, these two populations are roughly equal. The simulations predict that the GSS should comprise a total of 35% of the population in field f135, which is somewhat larger than the fraction of the total population in the most negative cold component

from the triple-Gaussian fit shown in Figure 14 (25%). If the “GSS” component from the triple-Gaussian fit is actually comprised of two narrower streams, the GSS comprises a much smaller percentage of the stars in this field than predicted by the simulations.

## 7.2. Arguments Against a Disk Origin

The substructure discovered in fields H11, f116 and f123 is centered at close to the systemic velocity of M31 ( $v_{\text{sys}} = -300$  km s $^{-1}$ ), which is also the radial velocity expected for an M31 disk component on the minor axis. Recent observational evidence suggests that M31’s stellar disk extends smoothly out to  $R_{\text{disk}} \sim 40$  kpc and has a velocity dispersion of  $\sim 30$  km s $^{-1}$ ; isolated features with disk-like kinematics have been observed as far out as  $R_{\text{disk}} \sim 70$  kpc (Reitzel et al. 2004; Ibata et al. 2005). We present three lines of evidence arguing against a disk origin for the  $\sim -300$  km s $^{-1}$  cold component found on the southeastern minor axis.

### DISK TO INNER SPHEROID SURFACE BRIGHTNESS RATIO

Previous measurements of M31’s stellar disk and inner spheroid (Walterbos & Kennicutt 1988; Pritchett & van den Bergh 1994) indicate that the disk constitutes a negligible fraction of the total light in our minor axis fields. Even in our innermost field f109 (at  $R_{\text{proj}} \sim 9$  kpc, corresponding to  $R_{\text{disk}} \sim 38$  kpc for a disk inclination of  $77^\circ$ ), the disk fraction is expected to be only  $\sim 10\%$  (Guhathakurta et al. 2005) based on disk scale radii of 5.0–6.0 kpc (Ibata et al. 2005). We see no evidence of a cold, disk-like feature in f109’s radial velocity distribution, although a  $\lesssim 10\%$  component could be difficult to detect. The disk fraction drops sharply at larger radii: for example, at the distance of our innermost field containing the  $\sim -300$  km s $^{-1}$  cold component, H11 ( $R_{\text{disk}} \sim 51$  kpc), the expected smooth disk fraction is  $\sim 1\%$  (Brown et al. 2006a).

Non-uniformities in M31’s stellar disk could result in a higher disk fraction in our fields. To explain the strength of the  $\sim -300$  km s $^{-1}$  cold component in field H11 ( $N_{\text{sub}}/N_{\text{tot}} = 44\%$ ), the disk would have to contain a  $45\times$  enhancement in this field relative to the smooth disk. Even more extreme disk enhancements are needed to explain the cold component in fields f116 and f123.

If there is a warp such that the outer disk is more face on than the inner disk (Ibata et al. (2005) find a best fit disk inclination angle of  $64.7^\circ$  from  $20 < R_{\text{disk}} < 40$  kpc), the effective disk radii of our fields will be smaller and the smooth disk contribution larger than in the above calculation. As an extreme example of a warp, we consider a disk of scale length 5.7 kpc whose inclination changes from  $77^\circ$  at small radii ( $R_{\text{disk}} < 20$  kpc) to  $60^\circ$  at large radii ( $R_{\text{disk}} > 20$  kpc). In this case, H11 is at  $R_{\text{disk}} \sim 35$  kpc while f123 is at  $R_{\text{disk}} \sim 47$  kpc. With this disk model, taking into account projection effects in the disk surface brightness (the surface brightness decreases as the disk becomes more face on) but ignoring dust effects, the expected disk fractions in fields f109, H11, f116, and f123 are 20%, 18%, 17%, and 10%, respectively. Thus, it would still require a  $\sim 2.5\times$  enhancement in the disk to explain the cold component in H11. More importantly, the 20% cold, smooth disk fraction predicted by this warp model in field f109 is inconsistent

with our radial velocity data (Fig. 6). This disk fraction estimate for the warp is optimistic (high) in that it does not account for the reduction in surface brightness that would be caused by any stretching associated with the putative warp.

#### VELOCITY DISPERSION

The measured velocity dispersion of the  $\sim -300$  km s<sup>-1</sup> cold component in fields H11 and f116 is  $\gtrsim 50$  km s<sup>-1</sup>, while the velocity dispersion of this component is only  $\sim 10$  km s<sup>-1</sup> in field f123. These measurements are significantly above and below, respectively, the typical velocity dispersion of 30 km s<sup>-1</sup> measured for the extended, disk-like structure by Ibata et al. (2005), for which they observe a range in velocity dispersions from  $\sim 20$ –40 km s<sup>-1</sup>. If the cold component in each of these three fields is from the disk, it would require a warp and non-uniformities in the disk that happen to have the observed triangular shape in the position-velocity plane (top panel of Figure 9).

#### STELLAR AGES AND METALLICITIES

If the  $\sim -300$  km s<sup>-1</sup> cold component is debris associated with M31’s extended disk, its stellar population should reflect this. However, a comparison of the stellar ages and metallicities of the H11 field with deep HST/ACS and ground-based imaging of disk-dominated M31 fields yields very different star formation histories. Obviously disturbed sections of M31’s disk (e.g., the Northern Spur and the G1 clump) show evidence of recent star formation ( $\sim 3$  Gyr ago in the Northern Spur and  $\sim 250$  Myr ago in the G1 clump; Ferguson et al. 2005), while deep HST/ACS imaging of field H11 reveals that very few of the stars are younger than 4 Gyr (Brown et al. 2003, 2006b). Brown et al. (2006b) find that their disk-dominated HST/ACS field H13d, located at 25 kpc along the northeastern major axis, contains a significantly younger and more metal-rich population than H11. In addition, Brown et al. (2006a) find very good agreement between the stellar populations of field H11 and an HST/ACS field on the GSS (H13s, discussed further in § 8).

The comparison of the stellar ages and metallicities of M31 disk fields vs. that of field H11 is complicated by several uncertainties. A radial gradient in disk properties could result in M31’s outer disk (in field H11) being more metal-poor and older than the inner parts of the disk. Also, the Brown et al. (2006b) HST/ACS field H13d likely includes multiple galactic components including spheroid and wrap-around debris from the progenitor of the GSS, although the radial velocity distribution indicates that M31’s disk is the dominant component in this field (see Fig. 9 of Kalirai et al. 2006a).

In conclusion, the observations disfavor an extended rotating disk model as the physical origin of the  $\sim -300$  km s<sup>-1</sup> cold component identified along M31’s southeastern minor axis. Although a disk origin for this substructure cannot be ruled out, it requires simultaneous contrivance of multiple properties of the disk to explain the observations: patchy disk structure (to explain the absence of an observed disk in f109), a warp and enhancement (which cannot be due to recent star

formation) of the disk to explain the strength of the cold component, an anomalously large velocity dispersion for fields H11 and f116 and a smaller than average velocity dispersion in field f123, and a significant radial gradient in the metallicity and age of the stellar disk populations. Compared to the elegance of the southeastern shelf interpretation based on F07’s simulations, which is a true prediction and explains the observed properties of the cold component in all the fields in which it is detected, the disk origin clearly fails the test of Occam’s razor for the most likely physical origin of the  $\sim -300$  km s<sup>-1</sup> cold component.

#### 8. IMPLICATIONS FOR THE INTERMEDIATE-AGE SPHEROID POPULATION

Brown et al. (2003, 2006a,b) present HST/ACS photometry of fields in M31 down to 1–1.5 magnitudes below the main-sequence turnoff. Our field H11 is coincident with the Brown et al. (2003) spheroid field (Fig. 2). The photometry presented in Brown et al. (2006a) is from a field on the GSS of Andromeda at a projected radial distance of 20 kpc, and is coincident with the Keck/DEIMOS spectroscopy field H13s presented in Kalirai et al. (2006a) and shown in Figure 12 ( $\xi = 0.3^\circ$ ,  $\eta = -1.5^\circ$ ). In the “smooth” spheroid field, Brown et al. (2003) find that  $\sim 30\%$  (by mass) of the stellar population is intermediate-age (6–8 Gyr) and metal-rich, while another 30% of the population is old (11–13.5 Gyr) and metal-poor. Brown et al. (2006a) find remarkable agreement in the CMDs of the stream and spheroid fields, indicating that the two fields have very similar age and metallicity distributions. They query whether the similarities between the populations could “be explained by the stream passing through the spheroid field,” but note that this explanation is problematic: the stream would have to dominate the spheroid by approximately the same factor in both fields (3:1 based on a kinematical analysis of the stream field H13s; Kalirai et al. 2006a), yet the kinematical profiles of the two fields are distinctly different, with the H11 field failing to show the cold ( $\sigma_v = 16$  km s<sup>-1</sup>) signature of the stream seen in the H13s field. However, they presciently suggested that the similarity in the two populations (spheroid and stream) implies that “the inner spheroid is largely polluted by material stripped from either the stream’s progenitor or similar objects.”

In light of the substructure presented in this paper, this seems to be the correct interpretation of the similarity between the “spheroid” and GSS stellar populations. The spatial and kinematic properties of the substructure suggest that the region of the spheroid imaged in the original HST field (Brown et al. 2003) is in fact contaminated by stars from the progenitor of the GSS. The kinematical signature of the substructure at the minor axis distance of the HST/ACS field (H11) is both predicted and observed to be relatively wide (Fig. 13), and thus less obvious against the underlying hot component. In the context of the F07 simulations, the minor axis substructure is not isolated, but is part of one of a series of shells caused by the disruption of the GSS’ progenitor, which collectively contaminate a large part of the inner spheroid of M31 (Fig. 12).

The current analysis suggests that  $\sim 45\%$  of the M31

RGB stars in the H11 field are in fact part of the  $\sim -300 \text{ km s}^{-1}$  cold component, and not part of the broad spheroid. In the H13s field, 75% of the M31 RGB stars are part of a cold component (Kalirai et al. 2006a). This difference in substructure fraction agrees nicely with the difference in the fraction of intermediate-age ( $< 10 \text{ Gyr}$ ), metal-rich stars found in the stream and spheroid fields in Brown et al. (2006b): 70% vs. 40%, respectively. However, recent HST/ACS observations of a field in the location of our f130 masks at 21 kpc imply that this is not the end of the story: Brown et al. (2007) find that the stellar population in H11 can *not* be fit by a linear combination of the GSS (H13s) and the 21 kpc spheroid (f130) stellar populations, due largely to the presence of a greater number of stars younger than 8 Gyr in H11 than in the GSS field. Nevertheless, the observational evidence, combined with the theoretical predictions of F07, strongly favor the explanation that the age and metallicity distributions of the stream and spheroid HST fields are so remarkably similar because the same progenitor polluted both fields with substructure.

## 9. SUMMARY

The use of the diagnostic method described in Gilbert et al. (2006) has enabled us to isolate the first sample of spectroscopically confirmed M31 RGB stars defined *without* the use of radial velocity. We use this sample of  $\sim 1000$  M31 RGB stars to measure the velocity dispersion of the inner spheroid of M31; in the radial range  $R_{\text{proj}} = 9 - 30 \text{ kpc}$  the inner spheroid has a velocity dispersion of  $\sigma_v^{\text{sph}} = 129 \text{ km s}^{-1}$ . Our data show no evidence of a decrease in the velocity dispersion over this radial range.

The stellar radial velocity distribution in these fields shows evidence of a significant amount of substructure. Compared to the large velocity dispersion seen in the underlying hot spheroid population, the substructure is kinematically cold, exhibiting a decrease in velocity dispersion with increasing projected radius. In the fields in which the  $\sim -300 \text{ km s}^{-1}$  cold component is observed,  $\approx 41\%$  of the stars are estimated to belong to it; the rest are members of the hot inner spheroid of M31. The metallicity of the substructure is higher than that of the broad spheroidal component in the fields in which it is observed.

The physical origin of the substructure discovered in this paper is most likely tidal debris stripped from the progenitor of the GSS. The data agree very well with the location and kinematical properties of the Southeast shelf predicted by the F07 simulations of the disruption of the GSS’ progenitor, and will add significant observational constraints to those already existing from the GSS, Northeast shelf, and Western shelf, enabling detailed modeling of M31’s dark matter distribution (F07). The minor axis fields also place constraints on the spatial distribution of the GSS itself. The GSS contamination in

our minor axis fields is much smaller than predicted by the current models of the stream (F07), which suggests the stream’s progenitor had a more complex structure than the spherical, non-rotating models used so far.

The newly-discovered substructure sheds light on the discovery of a significant intermediate-age population in the “smooth” spheroid field by Brown et al. (2003), and the subsequent discovery of the similarity in ages and metallicities of the stars in the spheroid field and a field on the GSS (Brown et al. 2006a,b). The spheroid HST/ACS field was not in fact placed on a “smooth” spheroid field, and the intermediate-age population may be part of the substructure observed in this field. If the substructure identified in this paper is indeed from the same progenitor as the giant southern stream, it is not surprising that the two HST/ACS fields would have very similar age and metallicity distributions. Given the number of observed fields in the inner spheroid which are contaminated by substructure, both in the current work and in the literature (Irwin et al. 2005; Ferguson et al. 2005; Kalirai et al. 2006a), it seems likely that the inner spheroid is highly contaminated by tidal debris. A “smooth” inner spheroid field may in fact be a rarity.

We are grateful to Sandy Faber and the DEIMOS team for building an outstanding instrument and to Mike Rich for his role in the acquisition of many of the Keck/DEIMOS masks. We thank Peter Stetson, Jim Hesser, and James Clem for help with the acquisition and reduction of CFHT/MegaCam images, Phil Choi, Alison Coil, Geroge Helou, Drew Phillips, and Greg Wirth for observing some DEIMOS masks on our behalf, Drew Phillips for help with slitmask designs, Jeff Lewis, Bill Mason, and Matt Radovan for fabrication of slitmasks, and the DEEP2 team for allowing us use of the `spec1d/zspec` software. We also thank Tom Brown for stimulating discussions and comments on the draft. The `spec2d` data reduction pipeline for DEIMOS was developed at UC Berkeley with support from NSF grant AST-0071048. This project was supported by an NSF Graduate Fellowship (K.M.G.), NSF grants AST-0307966 and AST-0507483 and NASA/STScI grants GO-10265.02 and GO-10134.02 (P.G., K.M.G., and J.S.K.), NSF grant AST-0205969 and NASA ATP grants NAGS-13308 and NNG04GK68G (M.F.), NSF grants AST-0307842 and AST-0307851, NASA/JPL contract 1228235, the David and Lucile Packard Foundation, and The F. H. Levinson Fund of the Peninsula Community Foundation (S.R.M., J.C.O., and R.J.P.) and NSF grant AST-0307931 (D.B.R.). J.S.K. is supported by NASA through Hubble Fellowship grant HF-01185.01-A, awarded by the Space Telescope Science Institute, which is operated by the Association of Universities for Research in Astronomy, Incorporated, under NASA contract NAS5-26555.

## APPENDIX

These appendices are intended to give the interested reader more insight into the origin of the differences in the distributions of the M31 RGB samples shown in Figure 3 (§ A.1). The amount of contamination vs. completeness for different  $\langle L_i \rangle$  thresholds is discussed in § A.2. Finally, in § A.3 we quantify the effect of the dwarf contamination on the radial velocity distributions for the M31 RGB sample used in this analysis.

### A.1 Effect of the Radial Velocity Diagnostic

As discussed in § 3, empirical probability distribution functions (PDFs) based on training sets of M31 RGB and MW dwarf stars are used to determine the probability that an individual star is an M31 red giant ( $P_{\text{giant}}$ ) or MW dwarf ( $P_{\text{dwarf}}$ ) in 4 (5 for field a0) diagnostics. These probabilities are used to compute the likelihood a star  $i$  is a red giant in a given diagnostic  $j$ :

$$L_{ij} = \log\left(\frac{P_{\text{giant}}}{P_{\text{dwarf}}}\right). \quad (1)$$

A star's overall likelihood of being an M31 RGB star is defined as

$$\langle L_i \rangle = \frac{\sum_j w_j L_{ij}}{\sum_j w_j}. \quad (2)$$

All available diagnostics for a star are given a weight of one, unless the star is an outlier with respect to both the M31 RGB and MW dwarf PDFs in a two-dimensional diagnostic, in which case the weight of that diagnostic is reduced (§ 3.3 of Gilbert et al. 2006).

Figure 16 shows the overall likelihood distributions for each field, both with ( $\langle L_i \rangle$ , *dashed histogram*) and without ( $\langle L_i \rangle_{\checkmark}$ , *solid histogram*) the radial velocity diagnostic included in the computation. In general, stars with  $\langle L_i \rangle > 0.5$  are designated secure M31 red giants and stars with  $\langle L_i \rangle < -0.5$  are designated secure MW dwarfs, while stars with  $0 < \langle L_i \rangle < 0.5$  are designated marginal M31 red giants and stars with  $-0.5 < \langle L_i \rangle < 0$  are designated marginal MW dwarfs (§ 3.5 of Gilbert et al. 2006).

Figure 3 shows the radial velocity distributions of several combinations of stars: only secure M31 RGB stars, secure and marginal M31 RGB stars, and secure M31 RGB stars plus all stars that are classified as marginal (M31 red giants and MW dwarfs), chosen by use of the diagnostic method both with and without the inclusion of the radial velocity diagnostic. Radial velocity is the most powerful single diagnostic, with a large range of  $P_{\text{giant}}/P_{\text{dwarf}}$  values (e.g., Fig. 10 and § 3.4 of Gilbert et al. 2006) and the ability to significantly boost the combined likelihood values. Thus, when the radial velocity diagnostic is not included in the overall likelihood calculation, the  $\langle L_i \rangle_{\checkmark}$  values are in general smaller, as can be seen in Figure 16. This causes the significant decrease in the number of secure M31 RGB stars in the top panel of Figure 3.

Stars near and more negative than the systemic velocity of M31 have a particularly high probability of being M31 RGB stars in the radial velocity diagnostic: stars with  $v_{\text{hel}} = -250 \text{ km s}^{-1}$  have an  $L_v = 2$  while stars with  $v_{\text{hel}} < -300 \text{ km s}^{-1}$  have  $L_v = 5$ . Consequently, the velocity diagnostic has a large affect on the  $\langle L_i \rangle$  values of these stars, and they are statistically the most affected by removing the radial velocity diagnostic from the overall likelihood calculation. Stars that have velocities in the range over which the radial velocity distributions of the M31 RGB and MW dwarf stars overlap ( $\approx -200 < v_{\text{hel}} < -125 \text{ km s}^{-1}$ ) will have likelihood values near 0 in the radial velocity diagnostic. This means two things: (1) since the  $L_v$  value is near zero, it adds no power to the  $\langle L_i \rangle$  determination, and thus the number of objects classified as secure M31 RGB stars should be similar regardless of whether or not the radial velocity diagnostic is used, and (2) since these stars do not have the power of the radial velocity diagnostic, they are statistically more likely to land in the marginal ( $-0.5 < \langle L_i \rangle < 0.5$ ) regime. The first effect can be seen in both the top and middle panels of Figure 3, and the second effect can be seen by comparing the numbers of stars in the shaded/dotted histogram in the range  $-200 < v_{\text{hel}} < -125 \text{ km s}^{-1}$  in the top, middle, and bottom panels.

The shifting of the overall likelihood distributions to smaller absolute  $\langle L_i \rangle$  values due to the removal of the radial velocity diagnostic also increases the numbers of marginal MW dwarf stars (and correspondingly decreases the number of secure MW dwarf stars). As in the case of the secure M31 RGB stars, removing the radial velocity diagnostic from the overall likelihood calculation will have the largest effect on stars that have radial velocities close to or more positive than the peak of the dwarf distribution (observed to be at  $v_{\text{hel}} \sim -50 \text{ km s}^{-1}$  in our data set; e.g., Fig. 2 of Gilbert et al. 2006). This causes stars that otherwise would be classified as secure MW dwarf stars to fall into the marginal ( $-0.5 < \langle L_i \rangle_{\checkmark} < 0.5$ ) or even secure ( $\langle L_i \rangle_{\checkmark} > 0.5$ ) M31 RGB regime, depending on the likelihood values of the other diagnostics. This boosts the number of stars in this velocity range in the M31 RGB samples selected without the inclusion of the radial velocity diagnostic.

### A.2 Selection of the M31 RGB Sample

Figure 3 shows that there is no difference in the velocity distributions of secure ( $\langle L_i \rangle > 0.5$ ) and secure plus marginal ( $\langle L_i \rangle > 0.0$ ) M31 RGB stars with  $v_{\text{hel}} < -300 \text{ km s}^{-1}$ , chosen with the use of the radial velocity diagnostic. Since there is minimal MW dwarf contamination at velocities this negative, we assume that the number of M31 RGB stars with  $\langle L_i \rangle > 0$  (465 stars) represents the true number of M31 RGB stars observed in this velocity range. This allows a calculation of the level of incompleteness in other samples. There are 446 stars with  $v_{\text{hel}} < -300 \text{ km s}^{-1}$  and  $\langle L_i \rangle_{\checkmark} > 0$ ; this sample is 96% complete. Samples selected using the thresholds  $\langle L_i \rangle_{\checkmark} > [0.5, 0.75, \text{ and } 1]$  are [78%, 57%, and 26%] complete.

The vast majority of the dwarf contaminants will have  $v_{\text{hel}} > -150 \text{ km s}^{-1}$ . Counts of stars in this velocity range for a given sample, compared to an estimate of the expected number of M31 RGB stars in this velocity range, gives an

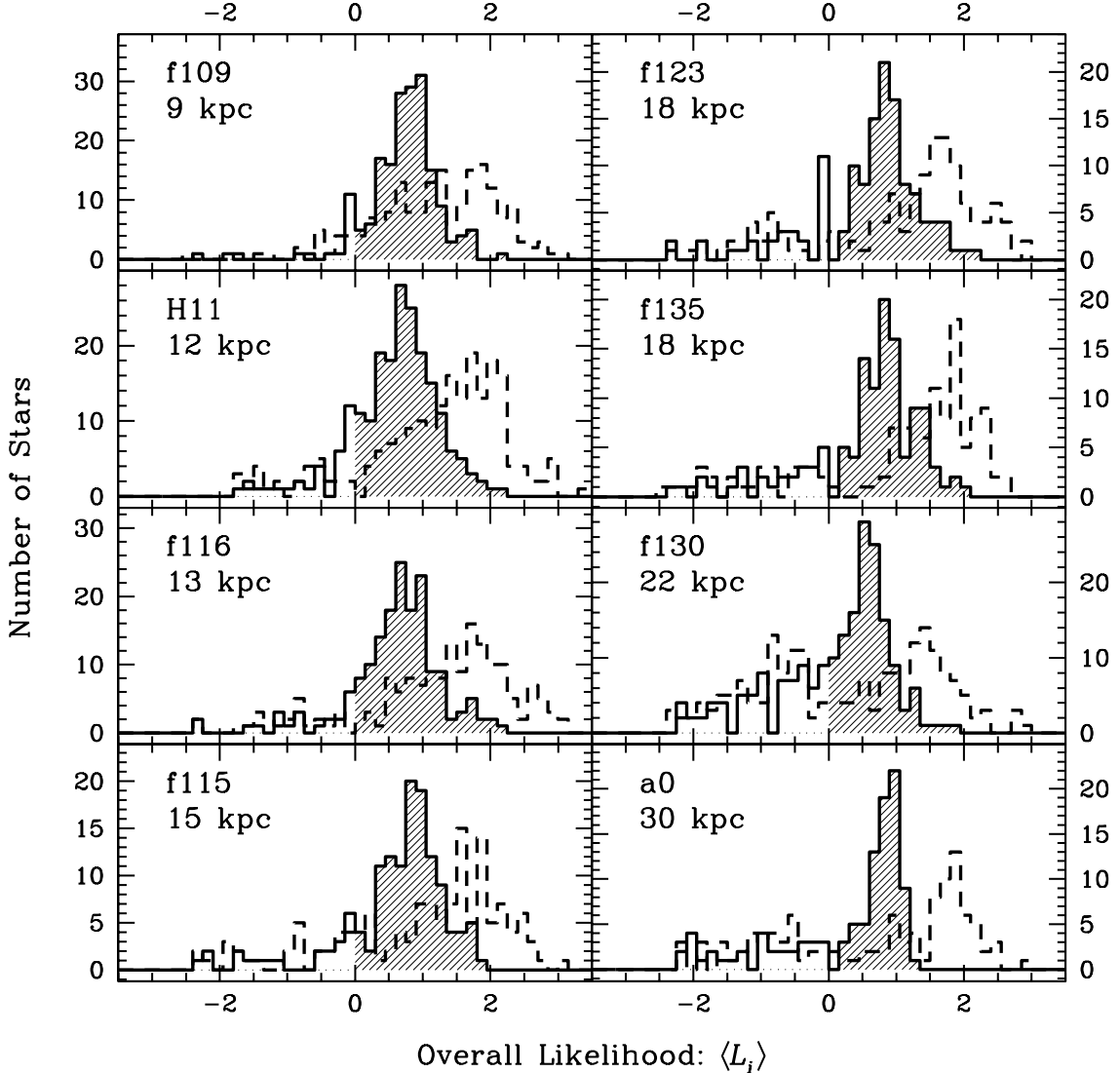


FIG. 16.— Overall likelihood distributions with ( $\langle L_i \rangle$ , *dashed*) and without ( $\langle L_i \rangle_{\psi}$ , *solid*) the inclusion of the radial velocity diagnostic. The analysis in this paper is based on the sample of M31 RGB stars shown by the shaded histograms. For stars with  $\langle L_i \rangle > 0$ , removal of the radial velocity diagnostic from the  $\langle L_i \rangle$  calculation causes a shift in the peak of the distribution from  $\langle L_i \rangle \simeq 2$  to  $\langle L_i \rangle \simeq 1$ . This is expected, since radial velocity is the most powerful of the five diagnostics. A similar shift of the peak of the distribution towards  $\langle L_i \rangle = 0$  likely occurs for stars with  $\langle L_i \rangle < 0$ , however the number of stars in this category is too small for this shift to be easily discernible.

estimate of the level of dwarf contamination. The thresholds  $\langle L_i \rangle_{\psi} > 0.75$  and  $\langle L_i \rangle_{\psi} > 1$  are quite severe, requiring that a star have a probability of being an M31 RGB star that is 5 or 10 times higher than its probability of being an MW dwarf star, respectively. These samples are assumed to have minimal dwarf contamination. Based on the numbers of stars with  $v_{\text{hel}} > -150 \text{ km s}^{-1}$  that pass these  $\langle L_i \rangle_{\psi}$  thresholds (41 stars for  $\langle L_i \rangle_{\psi} > 0.75$  and 22 stars for  $\langle L_i \rangle_{\psi} > 1$ ) and the completeness factors calculated above, a complete sample of M31 RGB stars would have approximately 76 stars at  $v_{\text{hel}} > -150 \text{ km s}^{-1}$ . A sample selected using the threshold  $\langle L_i \rangle_{\psi} > 0.5$  has 66 stars, which is 87% complete. However, the  $\langle L_i \rangle_{\psi} > 0.5$  sample is expected to be only 78% complete, implying that 9% of the stars with  $v_{\text{hel}} > -150 \text{ km s}^{-1}$  in this sample are MW dwarf star contaminants (overall, this sample has a 1.9% contamination rate). A similar calculation for stars selected using the  $\langle L_i \rangle_{\psi} > 0$  threshold yields a contamination rate of  $\sim 40\%$  for stars with  $v_{\text{hel}} > -150 \text{ km s}^{-1}$ . This large local contamination rate corresponds to only a 5.0% contamination rate for the entire sample. A parallel calculation using the number of stars with  $v_{\text{hel}} > -200 \text{ km s}^{-1}$  yields similar overall contamination rates, confirming that the majority of the MW dwarf contamination is at  $v_{\text{hel}} > -150 \text{ km s}^{-1}$ . The majority of the dwarf contamination comes from blue stars [panel (d) of Fig. 10], since the NaI, CMD, and [Fe/H] diagnostics are all less sensitive for blue stars (§ 4.1.2 of Gilbert et al. 2006).

The focus of this paper is the substructure discovered along the southeastern minor axis of M31. Therefore, we have chosen to use the most complete M31 RGB sample chosen without the use of radial velocity,  $\langle L_i \rangle_{\psi} > 0$ , as it gives

the most robust statistics for the cold component, even though it suffers from significant MW dwarf contamination at velocities near zero. The removal of the radial velocity diagnostic yields a sample composed of an underlying, kinematically unbiased M31 RGB population, as well as a contaminating MW dwarf population at velocities near zero. For the analysis presented in this paper, this is preferable to a clean, but kinematically biased M31 RGB sample, as the effect of the MW dwarf contamination on the measured properties of the M31 RGB sample can be quantified by analysing samples chosen using stricter  $\langle L_i \rangle_{\psi}$  thresholds.

### A.3 Bias in Measured Spheroidal Velocity

The main effect of the MW dwarf contamination in our chosen M31 RGB sample ( $\langle L_i \rangle_{\psi} > 0$ ) is a positive shift in the measured mean velocity of the spheroidal distribution. This shift will affect the measured  $\langle v \rangle^{\text{sph}}$  in the double-Gaussian fit to the combined sample (§ 4.1), and the  $\langle v \rangle^{\text{sph}}$  values from the single-Gaussian fits to individual fields (§ 4.2). The substructure component is cold enough that its measured properties are not significantly affected by the dwarf contamination. As discussed above (§ A.2), the amount of MW dwarf contamination is small in the  $\langle L_i \rangle_{\psi} > 0.5$  sample and minimal in the  $\langle L_i \rangle_{\psi} > 0.75$  sample. Although these samples suffer from significant incompleteness (22% and 43%, respectively), they are large enough to allow a measurement of the underlying spheroidal component. Maximum-likelihood double-Gaussian fits to the  $\langle L_i \rangle_{\psi} > 0.5$  and  $\langle L_i \rangle_{\psi} > 0.75$  samples yield  $\langle v \rangle^{\text{sph}}$  values of  $-302.5^{+7.7}_{-8.3}$  and  $-309.6^{+10.8}_{-8.7}$  km s<sup>-1</sup>, respectively. The best-fit  $\sigma_v^{\text{sph}}$  values for the two samples are  $123.3^{+8.3}_{-7.0}$  and  $128.3^{+10.8}_{-8.7}$  km s<sup>-1</sup>, respectively. Thus, the best-fit  $\langle v \rangle^{\text{sph}}$  values from the  $\langle L_i \rangle_{\psi} > 0$  sample should be adjusted by  $\sim 15$  to 20 km s<sup>-1</sup> to account for the MW dwarf contamination in the sample. This makes the  $\langle v \rangle^{\text{sph}}$  value from the best-fit double Gaussian ( $\langle v \rangle^{\text{sph}} = -287.2$  km s<sup>-1</sup>) consistent with the systemic velocity of M31 ( $v_{\text{sys}} = -300$  km s<sup>-1</sup>). Although the overall level of dwarf contamination is expected to increase with radius due to the decreasing surface density of M31 stars, there is little difference in the mean offset of  $\langle v \rangle^{\text{sph}}$  if the sample is split by radius into inner and outer bins.

### REFERENCES

- Abraham, R. G., van den Bergh, S., Glazebrook, K., Ellis, R. S., Santiago, B. X., Surma, P., & Griffiths, R. E. 1996, *ApJS*, 107, 1A
- Barnes, J. E., & Hernquist, L. 1992, *ARA&A*, 30, 705
- Battaglia, G., Helmi, A., Morrison, H., Harding, P., Olszewski, E. W., Freeman, K. C., Norris, J., Shectman, S. A. 2005, *MNRAS*, 364, 433
- Bertin, E., & Arnouts, S. 1996, *A&AS*, 117, 393
- Braun, R. 1991, *ApJ*, 372, 54
- Brinks, E. & Burton, W. B. 1984, *A&A*, 141, 195
- Brown, T. M., Ferguson, H. C., Smith, E., Kimble, R. A., Sweigart, A. V., Renzini, A., Rich, R. M., & Vandenberg, D. A. 2003, *ApJ*, 592, L17
- Brown, T. M., Smith, E., Guhathakurta, P., Rich, R. M., Ferguson, H. C., Renzini, A., Sweigart, A. V., & Kimble, R. A. 2006a, *ApJ*, 636, L89
- Brown, T. M., Smith, E., Ferguson, H. C., Rich, R. M., Guhathakurta, P., Renzini, A., Sweigart, A. V., & Kimble, R. A. 2006b, *ApJ*, 652, 323
- Brown, T. M., Smith, E., Ferguson, H. C., Guhathakurta, P., Kalirai, J. S., Rich, R. M., Renzini, A., Sweigart, A. V., Reitzel, D., Gilbert, K. M., & Geha, M. 2007, *ApJ*, in press (astro-ph/0702448)
- Bullock, J. S., & Johnston, K. V. 2005, *ApJ*, 635, 931
- Bullock, J. S., Kravtsov, A. V., & Weinberg, D. H. 2001, *ApJ*, 548, 33
- Chapman, S. C., Ibata, R., Lewis, G. F., Ferguson, A. M. N., Irwin, M., McConnachie, A., & Tanvir, N. 2006, *ApJ*, 653, 255
- Choi, P. I., Guhathakurta, P., & Johnston, K. V. 2002, *AJ*, 124, 310
- Conselice, C. J., Bershad, M. A., Dickinson, M., & Papovich, C. 2003, *AJ*, 126, 1183
- Croton, D. J., Springel, V., White, S. D. M., De Lucia, G., Frenk, C. S., Gao, L., Jenkins, A., Kauffmann, G., Navarro, J. F., & Yoshida, N. 2006, *MNRAS*, 365, 11
- de Vaucouleurs, G. 1958, *ApJ*, 128, 465
- Dekel, A., Stoehr, F., Mamon, G. A., Cox, T. J., Novak, G. S., & Primack, J. R. 2005, *Nature*, 437, 707
- Durrell, P. R., Harris, W. E., & Pritchett, C. J. 2004, *AJ*, 128, 260
- Fardal, M. A., Babul, A., Geehan, J. J., & Guhathakurta, P. 2006, *MNRAS*, 366, 1012F
- Fardal, M. A., Guhathakurta, P., Babul, A., & McConnachie, A. W. 2007, *MNRAS*, in press (astro-ph/0609050) [F07]
- Fellhauer, M., Belokurov, V., Evans, N. W., Wilkinson, M. I., Zucker, D. B., Gilmore, G., Irwin, M. J., Bramich, D. M., Vidrih, S., Wyse, R. F. G., Beers, T. C., & Brinkmann, J. 2006, *ApJ*, 651, 167
- Ferguson, A. M. N., Irwin, M. J., Ibata, R. A., Lewis, G. F., & Tanvir, N. R. 2002, *AJ*, 124, 1452
- Ferguson, A. M. N., Johnson, R. A., Faria, D. C., Irwin, M. J., Ibata, R. A., Johnston, K. V., Lewis, G. F., Tanvir, N. R. 2005, *ApJ*, 622, L109
- Ferguson, A. M. N., Chapman, S., Ibata, R. A., Irwin, M. J., Lewis, G. F., McConnachie, A. W. 2006, in Stanghellini, L., Walsh, J. R., Douglas, N. G., eds, *Planetary Nebulae beyond the Milky Way*. Springer-Verlag, Berlin, 286
- Font, A. S., Johnston, K. V., Guhathakurta, P., Majewski, S. R., & Rich, R. M. 2006, *AJ*, 131, 1436
- Geehan, J. J., Fardal, M. A., Babul, A., & Guhathakurta, P. 2006, *MNRAS*, 366, 996G
- Gilbert, K. M., Guhathakurta, P., Kalirai, J. S., Rich, R. M., Majewski, S. R., Ostheimer, J. C., Reitzel, D. B., Cenarro, A. J., Cooper, M. C., Luine, C., Patterson, R. J. 2006, *ApJ*, 652, 1188
- Guhathakurta, P. 2002, in “The Shapes of Galaxies and Their Dark Matter Halos”, ed. P. Natarajan (Singapore: World Scientific), 162
- Guhathakurta, P., Ostheimer, J. C., Gilbert, K. M., Rich, R. M., Majewski, S. R., Kalirai, J. S., Reitzel, D. B., & Patterson, R. J. 2005, arXiv preprint (astro-ph/0502366)
- Guhathakurta, P., Rich, R. M., Reitzel, D. B., Cooper, M. C., Gilbert, K. M., Majewski, S. R., Ostheimer, J. C., Geha, M. C., Johnston, K. V., & Patterson, R. J. 2006b, *AJ*, 131, 2497
- Helmi, A., & White, S. D. M. 1999, *MNRAS*, 307, 495
- Helmi, A., & de Zeeuw, T. 2000, *MNRAS*, 319, 657
- Helmi, A. 2004, *ApJ*, 610, L97
- Hernquist, L., & Quinn, P. J. 1998, *ApJ*, 331, 682
- Holland, S. 1998, *AJ*, 115, 1916
- Ibata, R., Chapman, S., Ferguson, A. M. N., Irwin, M., Lewis, G., & McConnachie, A. 2004, *MNRAS*, 351, 117
- Ibata, R., Chapman, S., Ferguson, A. M. N., Lewis, G., Irwin, M., & Tanvir, N. 2005, *ApJ*, 634, 287
- Ibata, R. A., Gilmore, G., & Irwin, M. J. 1994, *Nature*, 370, 194
- Ibata, R., Lewis, G. F., Irwin, M. J., Totten, E., & Quinn, T. 2001a, *ApJ*, 551, 294
- Ibata, R., Irwin, M. J., Ferguson, A. M. N., Lewis, G., & Tanvir, N. 2001b, *Nature*, 412, 49
- Innanen, K. A., Kamper, K. W., Papp, K. A., & van den Bergh S. 1982, *ApJ*, 254, 515
- Irwin, M. J., Ferguson, A. M. N., Ibata, R. A., Lewis, G. F., & Tanvir, N. R. 2005, *ApJ*, 628, 105
- Johnston, K. V., Hernquist, L., & Bolte, M. 1996, *ApJ*, 465, 278
- Johnston, K. V. 1998, *ApJ*, 495, 297
- Johnston, K. V., Hongsheng, Z., Spergel, D. N., & Hernquist, L., 1999, *ApJ*, 512, 109
- Johnston, K. V., Spergel, D. N., & Haydn, C. 2002, *ApJ*, 570, 656
- Johnston, K. V., Law, D. R., & Majewski, S. R. 2005, *ApJ*, 619, 800

- Kalirai, J. S., Guhathakurta, P., Gilbert, K. M., Reitzel, D. B., Rich, R. M., Majewski, S. R., & Cooper, M. C. 2006a, *ApJ*, 641, 268
- Kalirai, J. S., Gilbert, K. M., Guhathakurta, P., Majewski, S. R., Ostheimer, J. C., Rich, R. M., Cooper, M. C., Reitzel, D. B., & Patterson, R. J. 2006b, *ApJ*, 648, 389
- Law, D. R., Johnston, K. V., & Majewski, S. R. 2005, *ApJ*, 619, 807L
- LeFevre, O., Abraham, R., Lilly, S. J., Ellis, R. S., Brinchmann, J., Schade, D., Tresse, L., Colless, M., Crampton, D., Glazebrook, K., Hammer, F., & Broadhurst, T. 2000, *MNRAS*, 311, 565L
- Lotz, J. M., Davis, M., Faber, S. M., Guhathakurta, P., Gwyn, S., Huang, J., Koo, D. C., Le Floch, E., Lin, L., Newman, J., Noeske, K., Papovich, C., Willmer, C. N. A., Coil, A., Conselice, C. J., Cooper, M., Hopkins, A. M., Metevier, A., Primack, J., Rieke, G., & Weiner, B. J. 2007, *ApJ*, submitted (astro-ph/0602088)
- Majewski, S. R., Ostheimer, J. C., Kunkel, W. E., & Patterson, R. J. 2000, *AJ*, 120, 2550
- Majewski, S. R., Skrutskie, M. F., Weinberg, M. D., & Ostheimer, J. C. 2003, *ApJ*, 599, 1082
- Majewski, S. R., Frinchaboy, P. M., Kunkel, W. E., Link, R., Muñoz, R. R., Ostheimer, J. C., Palma, C., Patterson, R. J., Geisler, D. 2005, *AJ*, 130, 2677
- Mamon, G. A., & Łokas, E. L. 2005, *MNRAS*, 363, 705
- Martínez-Delgado, D., Gómez-Flechoso, M. Á., Aparicio, A., & Carrera, R. 2004, *ApJ*, 601, 242
- Mathewson, D. S., Cleary, M. N., & Murray, J. D. 1974, *ApJ*, 190, 291
- McConnachie, A. W., Irwin, M. J., Ibata, R. A., Ferguson, A. M. N., Lewis, G. F., & Tanvir, N. R. 2003, *MNRAS*, 343, 1335
- Merrett, H. R., Kuijken, K., Merrifield, M. R., Romanowsky, A. J., Douglas, N. G., Napolitano, N. R., Arnaboldi, M., Capaccioli, M., Freeman, K. C., Gerhard, O., Evans, N. W., Wilkinson, M. I., Halliday, C., Bridges, T. J. & Carter, D. 2003, *MNRAS*, 346, L62
- Merrett, H. R., Merrifield, M. R., Douglas, N. G., Kuijken, K., Romanowsky, A. J., Napolitano, N. R., Arnaboldi, M., Capaccioli, M., Freeman, K. C., Gerhard, O., Coccato, L., Carter, D., Evans, N. W., Wilkinson, M. I., Halliday, C., & Bridges, T. J. 2006, *MNRAS*, 369, 120
- Merrifield, M. R., & Kuijken, K. 1998, *MNRAS*, 297, 1292
- Mould, J. & Kristian, J. 1986, *ApJ*, 316, 517
- Navarro, J. F., Frenk, C. S., & White, S. D. M. 1996, *ApJ*, 462, 563
- Navarro, J. F., et al. 2004, *MNRAS*, 349, 1039
- Newberg, H. J., et al. 2003, *ApJ*, 596, L191
- Ostheimer, J. C. 2002, Ph.D. thesis, University of Virginia
- Peñarrubia, J., Benson, A. J., Martínez-Delgado, D., & Rix, H. W. 2006, *ApJ*, 645, 240
- Pritchett, C. J., & van den Bergh, S. 1994, *AJ*, 107, 1730
- Palma, C., Majewski, S. R., Siegel, M. H., Patterson, R. J., Ostheimer, J. C., & Link, R. 2003, *AJ*, 125, 1352
- Reitzel, D. B., & Guhathakurta, P. 2002, *AJ*, 124, 234
- Reitzel, D. B., Guhathakurta, P., & Rich, R. M. 2004, *AJ*, 127, 2133
- Rocha-Pinto, H. J., Majewski, S. R., Skrutskie, M. F., & Crane, J. D. 2003, *ApJ*, 594, L115
- Roberts, M. S. 1966, *ApJ*, 144, 639
- Schweizer, F. 1980, *ApJ*, 279, 596
- Searle, L., & Zinn, R. 1978, *ApJ*, 225, 357
- Sohn, S. T., Majewski, S. R., Muñoz, R. R., Kunkel, W. E., Johnston, K. V., Ostheimer, J. C., Guhathakurta, P., Patterson, R. J., Siegel, M. H., Cooper, M. C. 2007, *ApJ*, submitted (astro-ph/0608151)
- Springel, V., White, S. D. M., Jenkins, A., Frenk, C. S., Yoshida, N., Gao, L., Navarro, J., Thacker, R., Croton, D., Helly, J., Peacock, J. A., Cole, S., Thomas, P., Couchman, H., Evrard, A., Colberg, J., & Pearce, F. 2005, *Nature*, 435, 629
- Stanek, K. Z., & Garnavich, P. M. 1998, *ApJ*, 503, L131
- VandenBerg, D. A., Bergbusch, P. A., & Dowler, P. D. 2006, *ApJS*, 162, 375
- Walterbos, R. A. M., & Kennicutt, R. C., Jr. 1988, *A&A*, 198, 61
- White S. D. M., & Rees, M. J. 1978, *MNRAS*, 183, 341
- Yanny, B., et al. 2003, *ApJ*, 588, 824